Title

Transcriptional and epigenetic dysregulation impairs generation of proliferative neural stem and progenitor cells during brain aging.

Journal

Nature Aging, 4(1)

Authors

Li, Meiyang
Guo, Hongzhi
Carey, Michael
et al.

Publication Date

2024

DOI

10.1038/s43587-023-00549-0

Peer reviewed

HHS Public Access

Author manuscript

Nat Aging. Author manuscript; available in PMC 2024 July 04.

Published in final edited form as:

Nat Aging. 2024 January ; 4(1): 62–79. doi:10.1038/s43587-023-00549-0.

Transcriptional and epigenetic dysregulation impairs generation of proliferative neural stem and progenitor cells during brain aging

Meiyang Li[1,#], **Hongzhi Guo**[1,#], **Michael Carey**[2], **Chengyang Huang**[1,2]

[1.]Center for Neurobiology, Shantou University Medical College, Shantou 515041, China.

[2.]Department of Biological Chemistry, David Geffen School of Medicine at University of California at Los Angeles, Los Angeles, California 90095, USA.

Abstract

The decline in stem cell function during aging may affect the regenerative capacity of mammalian organisms; however, the gene regulatory mechanism underlying this decline remains unclear. Here we show that the aging of neural stem and progenitor cells (NSPCs) in the male mouse brain is characterized by a decrease in the generation efficacy of proliferative NSPCs, rather than the changes in lineage specificity of NSPCs. We reveal that the downregulation of age-dependent genes in NSPCs drives cell aging by decreasing the population of actively proliferating NSPCs, while increasing the expression of quiescence markers. We find that epigenetic deregulation of MLL complex at promoters leads to transcriptional inactivation of age-dependent genes, highlighting the importance of the dynamic interaction between histone modifiers and gene regulatory elements in regulating transcriptional program of aging cells. Our study sheds light on the key intrinsic mechanisms driving stem cell aging through epigenetic regulators and identifies potential rejuvenation targets that could restore the function of aging stem cells.

Aging of stem cells is a natural and inevitable biological process characterized by degenerative changes that are influenced by cell-intrinsic pathways and extrinsic factors within stem cell niches[1]. In the rodent brain, most neural stem and progenitor cells (NSPCs) with the ability to self-renew and differentiate into neurons persist in the subventricular zone (SVZ)[2, 3]. Within the SVZ, neural stem cells are identified as glial-like type B1 cells that can be activated to divide at a comparatively slower rate. The activated type B1 cells (type B1a) give rise to type C transit-amplifying progenitor cells that exhibit rapid division. Subsequently, the type C cells generate immature type A neuroblasts, which undergo further differentiation into neurons, thereby playing a crucial role in brain regeneration. The number of NSPCs and neurogenesis decrease in the aging brain[4–6]. Age-related NSPC defects

cyhuang@stu.edu.cn .

[#]Contributed equally to the study

Author contributions Statement

M.L. did most experiments and statistical analyses. H.G. performed the animal experiments. C.H. analyzed the bioinformatic data. C.H. and M.C. supervised the study.

Competing Interests Statement

The authors declare no competing interests.

have been implicated in cognitive impairment and neurodegenerative diseases[7], making the understanding of the molecular mechanisms underlying NSPC aging of utmost importance.

Transcriptional programs, regulated by dynamic complexes of sequence-specific transcription factors and epigenetic regulators, play a key role in NSPC proliferation and differentiation during brain development[8–11]. The lineage specificity of stem cells is a dynamic process determined during neural development and associated with genome-wide changes of both epigenetic marks and the transcriptome profile[12, 13]. Once determined, adult neural stem cells (NSCs) remain relatively quiescent to preserve the NSC pool in the brain SVZ but can be activated to become active NSPCs or proliferating cells during aging[14]. Transcriptional and epigenetic regulation have emerged as potential intrinsic mechanisms involved in NSPC aging, as evidenced by the study of age-related changes in the transcriptome and epigenome of SVZ tissues[15]. However, there is still a lack of the integrated analysis of age-related changes in both transcriptome and epigenome of aging NSPCs, as well as functional analyses of age-related genes, leaving it unclear whether they are causal factors or simply markers accumulated during the aging process. Moreover, how the loss of epigenetic modifications at gene-regulatory elements leads to the inactivation of age-dependent transcriptional programs and drives cell aging remains largely unknown.

This study reveals that NSPC aging is characterized by a decrease in the generation efficacy of proliferative NSPC, rather than a change in lineage specificity. This decline is linked to the downregulation of age-dependent genes and the epigenetic deregulation of the MLL complex, leading to decreased H3K4me3 signals at gene promoters and transcription inactivation. Our findings provide mechanistic insights into how the loss of epigenetic information drives the process of cell aging[16].

Results

Generation efficacy of proliferative NSPCs decreases in the aging brain.

To investigate the age-related decline of NSPC function in the brain, we evaluated NSPC proliferation in the SVZ of young (2 months) and aged (18 months) male mice. We administered BrdU to mice and labeled the active NSPCs in the SVZ using both BrdU and the NSPC marker SOX2[17-20]. The results showed that the percentage of BrdU and SOX2 double-positive NSPCs among SOX2-positive cells decreased in aged mice compared to young mice ($P < 0.005$), revealing a decline in the active NSPC population in the aging brain (Fig. 1a). We observed a decrease in the number of DCX and BrdU double-positive cells in aged mice compared to young mice, suggesting reduced NSPC neurogenesis during aging (Extended Data Fig. 1a). Overall, our findings suggest that NSPC activation for proliferation and differentiation becomes less efficient in the aging brain.

To verify the aging phenotype of NSPCs, we compared primary NSPCs from young (2 months) and aged (18 months) male mice, confirming similar expression levels of SOX2 and NESTIN in both groups (Extended Data Fig. 1b, c). Aged NSPCs formed fewer and smaller neurospheres than young cells (Fig. 1b, Extended Data Fig. 1d), and this trend persisted across subsequent generations (P1, P2, and P3). This suggests that NSPC self-renewal during aging might be controlled by a cell-intrinsic aging mechanism independent of an

in vivo niche. EdU labeling indicated a significant decrease in actively proliferating aged NSPCs, a trend that continued over time *in vitro* (Fig. 1d, e). While cell viability assays showed a decline in viable aged NSPCs, cell death rates remained low in both groups (Extended Data Fig. 1e, f). This suggests that the decreased number of viable NSPCs during aging is primarily attributed to reduced generation efficacy of proliferative NSPCs. Aged NSPCs were less efficient in differentiating into neurons but more likely to differentiate into astrocytes compared to young NSPCs (Extended Data Fig. 1g-i). Overall, our results provide evidence that aging NSPCs exhibit reduced efficacy in generating proliferative cells for self-renewal and differentiation into neurons.

To investigate age-related changes in the activation state and lineage progression of NSPCs at the molecular level, as well as identify genes that contribute to the reduced proliferation of NSPCs during aging, we performed single-cell transcriptomics analysis using the Chromium Single Cell 3' platform (10x Genomics). 5151 young and 4731 aged primary NSPCs that passed the quality control of the platform were used for data analysis. Using the Seurat package, we identified four distinct clusters (early type B1a cells, late type B1a cells, early type C cells, and late type C cells) in both young and aged NSPCs through integrated analysis of differentially expressed genes, NSPC quiescence and activation markers, as well as cell-type markers[21] (Fig. 1f, Extended Data Fig. 2a-d). Compared to type C cells, the activated type B1 cells (type B1a) display relatively lower levels of expression for activation markers (*Top2a*, *Mki67*, and *Mcm2*), while exhibiting higher expression of type B1 cell makers (*Slc1a3* and *Fabp7*)[22, 23]. Two activation states of type B1a cells were also identified, with the early state showing higher expression levels of quiescence markers (*Atp1a2*, *Aldoc*, *Apoe*, and *Cd9*) compared to the late state (Fig. 1g). The type C cells, particularly those in the late state of activation, display elevated expression levels of activation markers, as well as the type C cell marker *Ascl1*[24, 25]. Trajectory-based gene expression analysis of quiescence and activation markers, as well as pseudotime analysis using Monocle3[26] show the transition from slow-cycling type B1 cells to fast-cycling type C cells in both young and aged cell populations (Fig. 1h, Extended Data Fig. 2e). While the expression of NSPC lineage markers remained unchanged during aging (Extended Data Fig. 2c, d), our analysis revealed a higher proportion of late type B1a cells and a lower proportion of early type C cells in the aged group compared to the young group. However, the most quiescent and active NSPC proportions including early type B1a and late type C cells were similar between the aged and young cells (Fig. 1i). These results were consistent with the cell aging phenotype, suggesting that while the aged NSPCs could still be activated, their efficacy in generating proliferative NSPCs was lower in comparison to the young cells.

To investigate the age-related gene expression pattern in each NSPC cluster, we identified marker genes that were preferentially expressed in each NSPC cluster and further analyzed how these markers changed their expression between the aged and young NSPCs. Surprisingly, early type B1a had the most differentially expressed (DE) marker compared to the other clusters (Fig. 1j). Gene ontology (GO) analysis showed that the DE markers of early type B1a were involved in the regulation of localization (21 markers), cellular response to chemical stimulus (20 markers), and system development (22 markers) (Extended Data Fig. 2f). The *Aldoc* and *Atp1a2* genes, which have been previously found to be positively associated with NSC quiescence[27–29], were up-regulated in aged NSC populations in

agreement with the cell aging phenotype. The down-regulated genes, such as *Nrn1* and *Trf*, promote neuroregeneration and cell survival[30, 31] (Fig. 1k). GO annotations related to the DE markers of late type B1a cells include microtubule binding (*Map1b*), cytochrome-c oxidase activity (*Cox6a2*), nucleotide binding (*Elavl3*), DNA-binding transcription factor activity (*Atf5*), oxidoreductase activity (*Moxd1*), and carbohydrate binding (*Cntn1*). For early type C cells, GO annotations include signaling receptor binding (*Lpl*) and chromatin binding (*Hes5*). For late type C cells, GO annotations include DNA-binding transcription factor activity (*Mef2c* and *Pttg1*), and GTP binding (*Arl4c*). Further analysis using the DE marker *Hes5* in early type C cells revealed that the proportion of *Hes5*-positive early type C cells is lower in the aged cell population compared to the young cells. The reduced proportion of *Top2a*-positive early type C cells was also observed in the aged group (Fig. 1l-n). These findings provide insights into the stalling of the intermediate stage of NSPC activation during aging. Taken together, our results demonstrate a consistent decrease in the generation efficacy of proliferative NSPCs during aging, observed at both the cellular and molecular levels.

Downregulation of age-dependent genes drives NSPC aging.

To uncover the transcriptional mechanisms contributing to NSPC aging, we first performed bulk RNA sequencing to analyze the transcriptomic changes between the young and aged NSPCs isolated from the brain SVZ. Differential expression analysis identified 215 down-regulated genes and 208 up-regulated genes in the aged NSPCs compared to the young NSPCs (fold change >1.5 from three independent experiments) (Fig. 2a). GO analysis revealed that many differentially expressed genes in NSPC aging were involved in developmental processes and cell differentiation. The down-regulated genes displayed more enrichment with lower adjusted p-values in the development and differentiation compared with the up-regulated genes (Fig. 2b). Importantly, there were 42 down-regulated genes involved in nervous system development, such as *Dmrta2*, *Dlx2*, *En2*, and *Gjc1*, which have been implicated in regulating NSPC proliferation and differentiation in early brain development and might be related to NSPC aging phenotypes[32–35]. Our data link transcriptional downregulation of developmental genes to the process of NSPC aging.

To explore the link between transcriptional regulation and changes in aging phenotypes of NSPCs, we used a mouse model comparing control groups to those subjected to calorie restriction (CR), an anti-aging intervention[4, 36]. The result showed that the percentage of active NSPCs co-labeled with BrdU and *Sox2* in the young group increased from about 55% to 75% after the CR diet ($P < 0.05$), whereas no significant change was detected in the aged group (Extended Data Fig. 3a). CR increased neurogenesis in young mice but had no significant effect on neurogenesis in aged mice (Extended Data Fig. 3b). Consistent with *in vivo* results, cellular phenotype analysis revealed an increase in the self-renewal capacity of NSPCs isolated from the SVZ of young mice on CR versus those on AL, but this was not evident in aged NSPCs (Extended Data Fig. 3c, d). Transcriptomic analysis of NSPCs isolated from the SVZ of mice subjected to AL feeding or CR revealed a total of 26 age-dependent down-regulated genes and 6 up-regulated genes that exhibited transcriptional reversal in the CR-treated young mice compared to their AL-treated counterparts. Notably, among these age-dependent down-regulated genes, 16 were found to be involved in

developmental processes based on the GO analysis in Figure 2b. Moreover, we observed a greater number of age-dependent down-regulated genes displaying transcriptional reversal in the young group after calorie restriction, in contrast to the aged group (Extended Data Fig.3e, f). These results indicate an association between the aging phenotypes of NSPCs and the transcriptional regulation of developmental genes.

Next, we hypothesized that the functional decline of NSPCs might result from the inactivation of age-dependent genes identified in the above transcriptomic analysis. To test this hypothesis, we performed a functional RNAi screening using three sequence-independent siRNAs targeting each age-dependent down-regulated gene. A total of 156 siRNA sequences were designed to target 52 genes that were identified as developmental genes in the above GO analysis. Each siRNA was transfected into primary young NSPCs to observe its effect on cell viability. We found 82 siRNAs significantly reduced cell viability while only 12 siRNAs increased cell viability, as compared to the negative control group ($P < 0.05$) (Fig. 2c, d). To examine whether silencing of the age-dependent genes affects NSPC self-renewal, we performed a neurosphere formation assay two days post-transfection with siRNAs targeting 10 genes, including *Barhl2*, *Dmrta2*, *Hlx*, *Igf2bp2*, *Igf2bp3*, *Lix1*, *Nkain2*, *Tmem28*, *Trf*, and *Twist1* in young NSPCs. These genes are known for their role in development but with unclear effects on NSPC aging[34, 37–45]. Our results show that the number of neurospheres in each group was significantly decreased upon knockdown of these genes ($P < 0.05$) (Fig. 2e). Further analysis with EdU incorporation assay showed that silencing of these genes resulted in a decrease in the generation of actively proliferating NSPCs, closely resembling the characteristics of aged cells ($P < 0.05$) (Fig. 2f, g).

The age-dependent genes in the bulk RNA-seq were detected to different extents in the scRNA-seq data (Extended Data Fig. 4a). However, the read counts of are typically much lower than bulk RNA-seq, making it more difficult to detect the transcriptomic changes between the young and aged cell populations. However, several DE markers including the NSC quiescence markers *Atp1a2* and *Aldoc*, and the cell survival-related gene *Nrn1*, could be detected in the differential expression analysis ($P < 0.05$) (Extended Data Fig. 4b). The association between the upregulation of quiescence markers (*Aldoc* and *Atp1a2*) and the reduced generation efficacy of aged proliferative NSPCs promoted us to examine whether these markers could be used to validate the NSPC aging phenotype caused by the knockdown of age-dependent genes. Indeed, at least one of the markers could be up-regulated by the knockdown of each age-dependent gene (Extended Data Fig. 4c, d). Furthermore, we cloned a wild-type human *Igf2bp2* gene in an adenoviral plasmid that showed high homology with the mouse gene but was not targeted by *Igf2bp2* siRNA. The adenovirus-mediated transduction of *Igf2bp2* was performed 3 hours post-transfection of siRNAs in the young NSPCs. The EdU labeling after 2 days' transduction showed that the enhanced expression of the human *Igf2bp2* gene in the murine *Igf2bp2*-knockdown cells rescued the number of actively proliferating NSPCs (Fig. 2h, i). Overall, our data provide support for our hypothesis that downregulation of age-dependent genes drives NSPC aging.

Age-dependent genes are potential targets for rejuvenation of aging NSPCs.

Next, we examined the age-related changes in the expression of IGF2BP2, IGF2BP3, and BARHL2 in the SVZ. We selected these genes based on their consistent and robust cell phenotypes observed in the above *in vitro* assays. *In situ* immunofluorescence staining analysis showed that the percentage of IGF2BP2 and SOX2 double-positive cells significantly decreased within SOX2-positive cell population in the SVZ of aged mice, as compared to young mice (Fig. 3a). A similar reduction in the percentage of IGF2BP3+ SOX2+ and BARHL2+ SOX2+ cells within SOX2-positive cell population was observed in the SVZ of aging brain (Fig. 3b-c). It has been known that EGFR is highly expressed in active NSPCs including type B1a cells and type C cells in the SVZ[46]. We examined the expression profiles of these age-dependent genes in EGFR-positive NSPCs in the SVZ during aging. Immunofluorescence staining revealed a significant reduction in the percentage of IGF2BP2+EGFR+, IGF2BP3+EGFR+, and BARHL2+EGFR+ cells within EGFR+ NSPC population in aged mice compared to young mice (Fig. 3d-f). Collectively, our findings confirm the age-dependent downregulation of genes observed in the primary NSPCs derived from the SVZ of the aging brain.

To investigate whether the enhanced expression of age-dependent genes can rejuvenate the NSPC niche and improve the generation efficacy of proliferative NSPCs, we injected adenoviruses encoding Flag-tagged *Igf2bp2*, *Igf2bp3*, and *Barhl2* cDNA individually into the SVZ of aged mice. Within the SVZ, cells identified by NSPC marker SOX2 are the predominant cell population (Extended Data Fig. 5a). In contrast, other cell types, such as αSMA+ ependymal cells, lack both proliferative and neurogenic activities in the SVZ[47]. Given this, we focused on examining the rejuvenating effects of adenovirus-mediated gene transduction on this primary SVZ cell population identified by SOX2. We first assessed the transduction efficiency of the genes in SOX2+ NSPCs. Immunofluorescence co-labeling with anti-FLAG and anti-SOX2 antibodies indicated that the majority of NSPCs were transduced with these genes (Fig. 3g). Next, we analyzed NSPC activation in the SVZ by co-labeling with BrdU and SOX2 after the viral transduction. Active NSPCs were identified by quantifying BrdU and SOX2 double-postive cells. Our results showed that overexpression of *Igf2bp2*, *Igf2bp3*, and *Barhl2* significantly increased the number of active NSPCs in the aged SVZ as compared to the control groups (Fig. 3h-j) or the wild-type SVZ counterparts (Extended Data Fig. 5b-d). Further examination of EGFR+ cells in the SVZ confirmed a significant increase in the number of active NSPCs following the enhanced expression of *Igf2bp2*, *Igf2bp3*, and *Barhl2* (Fig. 3k-m). These findings indicate the rejuvenating effect of these genes on the generation of proliferative NSPCs. We investigated the effect of *Igf2bp2* and *Igf2bp3* on neurogenesis by quantifying the number of DCX-positive neuroblasts in the SVZ. Our results showed that both *Igf2bp2* and *Igf2bp3* genes significantly increased the number of DCX+ cells (Extended Data Fig. 5e, f), indicating their rejuvenating effect on neurogenesis in the aged mice.

To further examine the rejuvenating effects of age-dependent genes on aged NSPCs, we transduced primary aged NSPCs with the adenoviruses carrying the genes *Igf2bp2*, *Igf2bp3*, and *Barhl2* (Extended Data Fig. 5g-i). We assessed the effect of adenovirus transduction on the NSPC viability. Our results indicated minimal cell death caused by the adenovirus

transduction (Extended Data Fig. 5j, k). Through EdU incorporation assay, we found the adenovirus-mediated transduction of *Igf2bp2*, *Igf2bp3*, and *Barhl2* rejuvenated the aged NSPCs by increasing the proportion of actively proliferating cells, as compared to the control group (Fig. 3n). This finding is consistent with the in vivo phenotypes observed following the viral transduction of these genes, suggesting that age-dependent genes can directly regulate NSPC activation. Altogether, our data suggest that age-dependent genes are potential rejuvenation targets for aging NSPCs.

Changes in histone modifications at gene regulatory elements are related to transcriptional dysregulation of NSPC aging.

Histone modifications at cis-regulatory elements play important roles in the epigenetic regulation of gene transcription[48, 49]. To investigate whether epigenetic mechanisms might contribute to the transcriptional inactivation in NSPC aging, we profiled the principal regulatory histone marks at the promoters and enhancers of age-dependent genes using chromatin immunoprecipitation followed by sequencing (ChIP-seq). While genome-wide signals of H3K27me3 and H3K4me3 spanning all transcription start sites (TSSs) remain similar in young and aged NSPCs (Extended Data Fig. 6a), differences emerged at the promoters of age-dependent genes. Increased H3K27me3 signals (FC > 1.5), linked to gene repression, were found at down-regulated gene promoters in aged NSPCs (Fig 4a). Concurrently, we observed decreased H3K4me3 signals at the promoters of 26 down-regulated genes and increased signals at the promoters of 17 up-regulated genes in aged versus young NSPCs (FC > 1.5) (Fig. 4b). Notably, the average signals of H3K4me3 at the promoters of aging-dependent down-regulated genes were higher in young NSPCs (Fig. 4d). Pearson correlation analysis revealed a positive correlation in the change of transcription level with the change of H3K4me3 signals at the promoters of age-dependent genes, particularly down-regulated genes (Extended Data Fig. 6c). Our results demonstrate that the decrease in active histone modifications at promoter is associated with the downregulation of NSPC age-dependent genes.

H3K27ac is histone modification found at active enhancers. Gene enhancers with lower signals of H3K27ac may be inactive or poised in transcription[50, 51]. As expected, the average genome-wide signals of H3K27ac did not change at the enhancers of all genes in the aged versus young NSPCs (Extended Data Fig. 6b). However, the locus-specific decrease of H3K27ac could be observed at the enhancers of 13 age-dependent, down-regulated genes versus increased H3K27ac signals at 8 up-regulated genes (Fig. 4c). Consistently, the average signals of H3K27ac at the enhancers of down-regulated genes were significantly higher in young NSPCs as compared to aged NSPCs (Fig. 4e). In addition, the transcriptional change of age-dependent genes positively correlated with the change of H3K27ac signals at the enhancers (Extended Data Fig. 6d). These data confirm that the reduction of active histone marks at the regulatory elements is associated with transcriptional inactivation in NSPC aging.

Next, we analyzed the molecular functions of age-dependent genes that positively correlated with histone modification changes and identified three molecular categories: transcription factors, signaling factors, and membrane proteins (Fig. 4f). Interestingly, the increased

H3K27me3 and decreased H3K4me3 signals simultaneously appeared at the promoters of *Igf2bp2*, *Igf2bp3*, *Fam155a*, *Flt1*, and four genes encoding transcription factors (*Barhl2*, *Nkx3–2*, *Otx2*, and *Twist1*) (Fig. 4g). We identified six down-regulated genes (*Igf2bp2*, *Nuak1*, *Fam155a*, *Nkain2*, *Barhl2*, and *Dmrta2*) displaying increased H3K27me3 at promoters and decreased H3K27ac at enhancers (Fig. 4h), along with four other down-regulated genes exhibiting decreased H3K4me3 and H3K27ac at these regions (Fig. 4i). These data suggest that interactions of different histone modifications at promoters and enhancers likely regulate transcription of age-dependent genes. Notably, the rejuvenation targets of aging NSPCs, including *Barhl2* and *Igf2bp2*, were highly associated with the dynamic changes in histone modifications during NSPC aging (Fig 4j), suggesting that they were potential targets of epigenetic regulators.

Histone modifications are associated with chromatin accessibility[52]. We expanded our analysis of regulatory elements of age-dependent genes using the ‘assay for transposase-accessible chromatin with sequencing’ (ATAC-seq)[53]. ln line with the results of H3K4me3 and H3K27ac profiles, the average profiles of chromatin accessibility at promoters and enhancers of all genes remain unchanged between the young and aged NSPCs, supporting the notion that stable chromatin states at the genome-wide level may be beneficial to the maintenance of NSPC identity during aging (Extended Data Fig. 6e, f). Locus-specific ATAC-seq changes were found at 14 promoters and 6 enhancers of age-dependent genes (Extended Data Fig. 7a). 10 age-dependent genes, including *Igf2bp3*, *Twist1*, *Igf2bp2*, *Otx2*, and *Barhl2*, which displayed reduced chromatin accessibility at their promoters, also displayed lower H3K4me3 signals at the same loci in the aged versus young NSPCs (Extended Data Fig. 7b, e; also see Fig. 4j). Reduced chromatin accessibility and H3K27ac could be found at 6 enhancers of age-dependent genes (Extended Data Fig. 7c). The chromatin accessibility and H3K4me3 at the promoters of NSPC lineage markers and housekeeping genes did not change during aging (Extended Data Fig. 7d). This observation is consistent with the cell phenotypic results showing that the NSPC lineage specificity does not change during aging, which in turn reinforces the concept that only the generation efficacy of proliferative NSPC is regulated by the age-related transcriptional and epigenetic programs in the aging cells.

To further investigate the age-related changes in histone modifications at gene promoters of NSPCs during brain aging, we employed the fluorescence-activated cell sorting (FACS) method to isolate EGFR+ NSPCs from both young and aged SVZ tissues in the brains (Extended Data Fig. 8a). The isolation of EGFR+ type B1a cells and type C cells enables a comparison of histone modification profiles with those obtained from primary NSPC-derived neurospheres[46]. Subsequently, we utilized the cleavage under targets and tagmentation (CUT&Tag) technique followed by sequencing to profile the histone mark H3K4me3 in the sorted NSPCs. Our results indicate that the average H3K4me3 profiles at all promoters remained unchanged between young and aged EGFR+ NSPCs (Extended Data Fig. 8b). The levels of H3K4me3 signals at the promoters of NSPC lineage markers did not exhibit any significant changes during aging (Extended Data Fig. 8c). Consistent with the findings obtained from NSPC-derived neurospheres, we observed locus-specific decreases in H3K4me3 levels at the promoters of 19 age-dependent down-regulated genes (FC > 1.5) (Extended Data Fig. 8d, e). The top 10 genes with reduced H3K4me3 signals in aged versus

young EGFR+ NSPCs also exhibited decreased expression levels (Extended Data Fig. 8f). Taken together, our findings suggest that epigenetic dysregulation plays a critical role as a cell-intrinsic mechanism underlying aging in NSPCs.

Identification of MLL complex as a key epigenetic regulator in functional decline of aging NSPCs.

Next, we aimed to identify epigenetic regulators that contribute to functional decline of NSPCs and transcriptional dysregulation during aging. We applied functional RNAi screening with 48 siRNAs targeting 16 epigenetic regulators to examine the cell viability upon gene knockdown. These epigenetic regulators are involved in regulation of histone H3 lysine 4 methylation (including *Kmt2a*, *Kmt2b*, *Kmt2c*, *Kmt2d*, *Ash2l*, *Dpy30*, *Rbbp5*, *Wdr5*, *Kdm1a*, and *Kdm5a*), histone H3 lysine 27 methylation (including *Ezh2*, *Jmjd3*, *Utx*, and *Uty*), and histone H3 lysine 27 acetylation (including *P300* and *Hadc1*). The results showed that the knockdown of MLL complex subunits (KMT2D, RBBP5, and WDR5) decreased cell viability, while the effects of interference by other epigenetic regulators were milder or negative (Fig. 5a-d). The MLL complex contains the catalytic subunit KMT2D and the common core subunits (ASH2L, DPY30, RBBP5, and WDR5)[54]. This complex has been found to catalyze H3K4 methylation at gene promoters[55, 56], but its function in NSPC aging is unknown. To validate the contribution of *Kmt2d*, *Rbbp5*, and *Wdr5* to the functional decline of aging NSPCs, we analyzed neurosphere formation upon knockdown of these genes in young NSPCs and found that the number of neurospheres significantly decreased 2 days post-transfection (Fig. 5e). Further analysis with EdU incorporation assay revealed that knockdown of KMT2D, RBBP5, and WDR5 decreased the number of actively proliferating NSPCs in neurospheres (Fig. 5f, g). Cell death rates remained low after the knockdown of these subunits (Extended Data Fig. 9). These results suggest that loss of function of MLL complex may drive aging of NSPCs by reducing cell proliferation and self-renewal capacity.

The expression of KMT2D, RBBP5, and WDR5 remained unchanged in young versus aged NSPCs consistent with the global effects of H3K4me3 observed in the aging NSPCs (Fig. 5h). This observation implied that the chromatin binding activity of MLL complex might change at the promoters of age-dependent genes during NSPC aging. We confirmed the specificity of KMT2D antibody through immunoprecipitation and mass spectrometry (IP-MS), which showed the enrichment of KMT2D and the MLLcomplex's core subunits. Surprisingly, however, we identified CBX3 (HP-1gamma) as a potentially new component interacting with the MLL complex (Extended Data Fig. 10a). We previously showed that CBX3 was a component of the RNA polymerase II preinitiation complex regulating the transcription of neural genes[9]. Reciprocal IP-MS analysis with the CBX3 antibody confirmed the interaction between CBX3 and the MLL complex[57] (Extended Data Fig. 10b). Next, we used ChIP-seq of MLL complex and CBX3 in young and aged NSPCs to analyze their binding activity at promoters of age-dependent genes displaying decreased H3K4me3 signals during aging. We found decreased enrichment of MLL complex at 15 promoters of age-dependent genes accompanied by decreased H3K4me3 signals in the aged NSPCs as compared to the young NSPCs (FC > 1.5), whereas the enrichment of CBX3 at most promoters remained unchanged or slightly altered (Fig. 5i, j). The relatively stable binding of CBX3 and the decreased binding of MLL complex suggested that the interaction

between MLL complex and CBX3 might be affected during NSPC aging. Indeed, CBX3 immunoprecipitation analysis revealed that the relative amount of KMT2D and RBBP5 decreased in the aged versus young NSPCs (Extended Data Fig. 10c). The data suggest that the binding activity of the MLL complex at gene promoters is regulated in aging NSPCs, and that the decreased binding of the MLL complex at promoters may contribute to the inactivation of the age-related transcriptional program.

Epigenetic deregulation of MLL complex at promoters leads to transcriptional inactivation of age-dependent genes.

We therefore explored the contribution of the MLL complex to the transcriptional and epigenetic inactivation of age-dependent genes during NSPC aging. We focused on *Barhl2*, *Igf2bp2*, and *Igf2bp3* genes because of their important roles in NSPC aging observed above (Fig. 2, 3). ChIP-qPCR analyses confirmed the decrease of MLL complex enrichment at the promoters of these genes (Fig. 6a-f). Knockdown of MLL complex subunits reduced the expression levels of *Barhl2*, *Igf2bp2*, and *Igf2bp3* (Fig. 6g-l), while the H3K4me3 signals at their promoters were also decreased in the MLL complex-knockdown versus control groups (Fig. 6m-r). Cell functional analyses showed that the increased expression of *Barhl2* and *Igf2bp2* genes in KMT2D-knockdown and RBBP5-knockdown cells, respectively, rescued the number of actively proliferating NSPCs (Fig. 6s). Collectively, these results support the concept that epigenetic deregulation of MLL complex at promoters leads to transcriptional inactivation of age-dependent genes of NSPCs.

Discussion

In this study, we report that aged NSPCs are more resistant to activation than young NSPCs but maintain the abilities to proliferate and differentiate to preserve the stem cell pool for regeneration in the aging brain. As opposed to the concept that aging cells undergo a broad change in the transcriptome, our data demonstrate that transcriptional dysregulation of NSPC aging occurs in a small group of genes that were previously found to be involved in developmental processes[32–35], whereas marker genes for lineage specificity remain unchanged with age. Instead of transgenic mice in which genomic and transcriptomic profiles might be modified in cells, the application of non-transgenic mice allows us to discover age-dependent genes of NSPCs in an “age-only” scenario. Transcriptional inactivation of the age-dependent downregulated genes results in cell aging by decreasing the number of active NSPCs while increasing the expression of quiescence markers. Our findings establish a causal relationship between the downregulation of developmental genes and the functional decline observed in aging NSPCs. The transcriptional inactivation decreases gene expression level, reflecting the accumulation of aging markers during NSPC aging. The effect of transcriptional inactivation on the generation efficacy of proliferative NSPCs and their self-renewal indicates that the age-dependent transcriptional program actively regulates the process of NSPC aging. Given the critical role of cell cycle in NSPC proliferation, future studies should focus on exploring the interplay between cell cycle regulation and transcriptional dynamics in NSPC aging. Although deficits in cell cycle progression have been observed in both synchronized and non-synchronized aged

neural progenitor cells[58], more research is needed to assess the potential influence of cell synchronization on the transcriptional patterns of age-related genes.

The rejuvenating effects of age-dependent genes, including *Igf2bp2*, *Igf2bp3*, and *Barhl2*, on aged NSPCs reinforce the important role of gene regulation in NSPC activation, This suggests a potential therapeutic approach for cell rejuvenation in the aging brain. Although *in vivo* viral vectors for gene delivery and transduction offer a potent methodology for studying the rejuvenating effects of age-dependent genes on aged NSPCs, it is critical to address associated technical hurdles, such as ensuring delivery specificity. Future research is needed to develop methods for cell-type-specific gene expression in the brain. Such advancements will provide more insights into both cell autonomous and non-autonomous mechanisms that regulate NSPC activation in the aging brain. Precise targeting of NSPCs during viral delivery of age-dependent genes can minimize off-target effects on other cell types in the brain, enhancing the consistency and reliability of gene therapy in cell rejuvenation studies.

Previous reports showed that widespread changes in epigenetic modifications and expression of epigenetic regulators occurred during the aging of hematopoietic stem cells and muscle stem cells[59, 60]. However, the age-associated changes in epigenomic profile occur in a cell-type-specific manner. Indeed, our study demonstrates that genome-wide histone modifications and chromatin accessibility at promoters and enhancers remain relatively stable during NSPC aging, which is important for self-renewal of stem cells and maintenance of lineage specificity. However, the decrease in active histone modifications, including H3K4me3 and H3K27ac at promoters and enhancers, respectively, was associated with transcriptional inactivation of age-dependent genes in aging NSPCs that exhibited a decreased capacity to generate actively proliferating cells. The concurrent reduction of chromatin accessibility at both promoters and enhancers of age-dependent genes suggests that epigenetic remodeling might contribute to in transcriptional inactivation during NSPC aging. Our study provides evidence supporting the concept that aging NSPCs undergo loss of chromatin accessibility at specific genes involved in the regulation of NSPC activity[61]. Notably, this loss of chromatin accessibility was observed at different stages of NSPC activation, including the transition from quiescent type B1 cells to activated type B1 cells, as well as the subsequent progression to rapidly dividing type C cells.

The binding activity of transcription and epigenetic regulators at the target promoters is involved in gene expression programs in self-renewal and cellular differentiation[9, 57, 62–64], but has not been found to regulate the stem cell aging so far. We identified the MLL complex as a critical epigenetic regulator of age-dependent transcriptional program in NSPCs. The decreased DNA binding activity of the MLL complex at the promoters of age-dependent genes, such as *Barhl2* and *Igf2bp2*, in aged NSPCs may result in decreased promoter H3K4me3 and transcriptional inactivation, which drives cell aging. Our results reveal the intriguing role of the dynamic interaction between epigenetic regulators and gene regulatory elements in regulating the transcriptional program of aging NSPCs, providing mechanistic insight into how the loss of epigenetic information drives the process of cell aging. This study extends our understanding of epigenetic and transcriptional mechanisms in stem cell aging and identifies potential rejuvenation targets for the aging cells. While the decreased

DNA binding activity of the MLL complex at gene promoters is independent of its protein level in aging NSPCs, it would be interesting to investigate the impact of age-related change in the protein levels of transcription or epigenetic regulators on downstream gene transcription and NSPC function during aging. Previous studies have shown that the reduced expression of transcription factor *Nrf2* mediates the age-related decline in NSPC function[65], while overexpression of *Nrf2* enhances NSPC function[66]. These findings highlight the important role of age-related change in the expression of transcriptional regulator in the process of NSPC aging. Future studies will be required to examine the *in vivo* effects of knocking down epigenetic and transcriptional regulators, such as the MLL complex, on the function of NSPCs in the SVZ.

While our study primarily focused on NSPCs in the SVZ, it is important to note that NSPCs in the hippocampal subgrandular zone (SGZ) exhibit distinct features compared to SVZ NSPCs. Unlike their SVZ counterparts, SGZ NSPCs are located away from ventricular walls and uniquely express the *Hopx* gene. These findings indicate important cellular and molecular differences between NSPCs in the SVZ and SGZ regions[67]. While Plagl2 and Dyrk1a were not age-dependent in SVZ NSPCs, altering their expression rejuvenated aged hippocampal stem cells[68]. This emphasizes the need to explore region-specific mechanisms in NSPC aging. In our study, we focused on male mice to avoid sex-related variations, but this limited the broader applicability of our results. Including female mice in future research is essential for a comprehensive understanding of transcriptional and epigenetic dysregulation in brain aging.

Methods

Mice

C57BL/6 male mice were maintained in a pathogen-free animal facility at Shantou University Medical College and were on a 12 h light/12 h dark cycle. Temperature for housing the mice was between 22°C to 25°C. Humidity for mice housing was around 50%. All the experiments using mice were approved and regulated by the Animal Welfare and Ethical Committee of Shantou University Medical College. In the group of ad libitum diet, mice had unlimited access to food. Calorie-restricted mice had less chow in a stepwise procedure, in which they received a 20% restriction in food in the first week and a 30% restriction from week 2 to week 5. All mice were provided continuous free access to water. The number of mice used in this experiment was as follows: seven mice in young AL group; seven mice in young CR group; eight mice in aged AL group; eight mice in aged CR group.

Stereotactic injection

The stereotactic injection was performed to deliver high titer adenovirus encoding *Igf2bp2*, *Igf2bp3*, and *Barhl2* genes into the SVZ of mouse brains. Control mice were injected with control adenovirus without expressing these three genes. During the surgical process, aged mice (18 months) were anesthetized intraperitoneally with pentobarbital sodium (80 mg/kg). After shaving the heads using an electric razor, mice were placed into a stereotactic apparatus (RWD Life Science, Shenzhen, Cat. No. 68030). Craniotomy and injection were performed as published[69]. 1.5 μl of adenovirus with a titer of 1 × 10^10

PFU/ml were injected into the SVZ using a glass microelectrode (VitalSense Scientific Instruments, Wuhan, Cat. No. B15024N) connected to a 5-μl microsyringe (RWD Life Science, Shenzhen, Cat. No. 79015). The injection rate was 0.13 μl per minute controlled by a microinjection syringe pump (Lead Fluid Technology, Hebei, Cat. No. TFD03–01). The stereotactic injection coordinates were: 0.5 mm anteroposterior (AP), 1.5 mm mediolateral (ML), and 2.5 mm dorsoventral (DV). The number of mice was as follows: four mice per control group; three mice per gene overexpression group.

Adenoviral production and quantification

The coding regions of DNA sequences of *Igf2bp2* (NM_006548), *Igf2bp3* (NM_006547), and *Barhl2* (NM_020063) genes were cloned into the adenoviral vector pAdM-FH (Vigene Biosciences) containing a C-terminal Flag tag. Viral packaging was performed by Vigene Biosciences. For the measurement of adenoviral titer, 10-fold serial dilutions of the viral samples were prepared from 10^{-2} to 10^{-7} and were added dropwise to each well of HEK 293 cells (WZ Biosciences) in a 96-well plate. After 48 h, transduced cells were fixed with ice-cold 100% methanol and incubated with an anti-Hexon antibody followed by incubation of a secondary antibody conjugated with horseradish peroxidase (HRP). The signals were detected with DAB staining. Plaque Forming Units (PFU) were calculated as follows: pfu/ml = (plaque numbers in the 10^{-6} well + plaque numbers in the 10^{-7} well × 10) × 1000/2/viral volume in the 10^{-6} well.

NSPC isolation and culture

Primary NSPCs were isolated from the brain SVZ of young male mice (2 months, n = 6) and aged male mice (18 months, n = 6), respectively, using a previously published protocol[70]. Briefly, the microdissection of the brain SVZ was performed on ice. The tissue pieces of SVZ from the group of mice were pooled and dissociated into single cells using the Neural Tissue Dissociation kit (Miltenyi Biotec, #130–092-628). The isolated cells were maintained in the initial proliferation medium containing 2% B27 supplement serum (Gibco, #17504044), 1% GlutaMax (Gibco, #35050–038), 20 ng/μl of human FGF basic growth factor (Sino Biological), 20 ng/μl of human EGF (Sino Biological), and 1% penicillin-streptomycin (Gibco, #15140122). The 3D suspension culture of primary NSPCs was performed in a petri dish (Jet Biofil) at 37°C and 5% CO_2 . Cells used for downstream experiments were within the passage range of P0 to P3. Cell images were acquired with EVOS FL Cell Imaging System (Thermo Fisher Scientific).

Neural differentiation of NSPCs

Primary NSPCs were isolated from the SVZ of young male mice (2 months, n = 6) and aged male mice (18 months, n = 6), respectively. These cells were then cultured in initial proliferation medium in a petri dish for 3 days to form neurospheres. On day 4 of culture, the neurospheres were transferred to neural differentiation medium, which consisted of neurobasal medium (Gibico, #21103049), 2% B27 (Gibco, #17504044), 1% N2 (Gibco, #17502048), and 1× GlutaMAX. The neurospheres were incubated in this medium for 48 hours. Subsequently, the neurospheres were seeded onto a tissue culture plate (NEST Biotechnology) coated with Poly-D-lysine (PDL, Sigma, #P7280) for adherent cell

differentiation. The adherent cells were cultured in fresh neural differentiation medium for an additional 2–4 days.

Fluorescence-activated cell sorting (FACS)

Single cell suspensions were prepared from the SVZ of young male mice (2 months, n = 4) and aged male mice (18–20 months, n = 4), respectively, using the described method[70]. The cell suspension was then incubated with 7-amino actinomycin D (7-AAD, ThermoFisher, #00–6993-50) for 15 min to label dead cells. After being washed with cold PBS buffer containing 1% BSA, the cells were incubated with biotinylated EGF complexed with Alexa Fluor 488 streptavidin (2 μg/mL, ThermoFisher, # E13345) for 30 min. FACS was performed using a BD FACSAria II flow cytometer with a setting of 13 psi pressure and a 100-μm nozzle aperture. The FACS Data were analyzed using FlowJo (V10) data analysis software.

RNAi assay

siRNA transfection into the cells was performed following a method published previously[9]. Briefly, single-cell suspension NSPCs were prepared by the dissociation of primary neurospheres from young mice. Lipofectamine RNAiMAX reagent was diluted in DMEM/F12 medium and mixed with the diluted siRNAs. The final concentration of siRNAs was 0.2μM. The siRNA-lipid complex was incubated for 5 minutes at RT before being added to the cells. The transduced cells were cultured for 48 hours at 37°C and 5% CO_2 before being used for assays. All siRNAs were synthesized by Ribo Life Science Co., Ltd. siRNA target sequences are shown in Supplementary Table 2.

Immunofluorescence staining

Transcardiac perfusion of mice was performed with ice-cold saline followed by 4% paraformaldehyde (PFA) solution (Sigma, #158127). The preserved brains were collected and fixed in 4% PFA solution for 2 hours followed by dehydration treatment in 30% sucrose at 4°C. The coronal section of the brain containing the region of lateral ventricle was embedded in O.C.T. compound (Tissue-Tek) in cryomolds and frozen at −80°C. 15 μm coronal cryosections of brains were prepared using a Leica CM1950 cryostat. The coronal sections containing SVZs on a microscope slide were blocked for non-specific antigens with PBS containing 5% BSA and 0.5% Triton X-100 for 1 hour at room temperature (RT). The sections were incubated with the primary antibody in PBS containing 1% BSA overnight at 4°C followed by staining with secondary antibody conjugated to fluorescence dye (1:800) for 2 hours at RT. The fluorescence signals were imaged using Zeiss LSM800 confocal laser scanning microscopy. The quantification of confocal fluorescent image was performed using Zeiss ZEN 2.6 blue edition software. The number of Sox2, Igf2bp2, Igf2bp3, and Barhl2 positive cells were counted across the lateral, dorsolateral, and dorsal SVZ, while the number of DCX and Flag positive cells were counted across the lateral and dorsolateral SVZ.

For cell immunostaining, cells cultured *in vitro* were fixed in 4% PFA solution for 20 min at room temperature and washed twice with PBS. Cell permeabilization and blocking were performed for 30 min at room temperature with PBS containing 0.1% Triton X-100

and 1% BSA. The incubation of the primary antibody and secondary antibody (1:800) was performed overnight at 4°C and then for 1 hour at RT. After washing the sections with PBS four times, the nuclei were stained with DAPI. Cells with indirect immunofluorescence signals in each sample were imaged using EVOS FL Cell Imaging System (Thermo Fisher Scientific). Images were captured to include a majority of the cells within each sample, with the goal of covering a representative portion of the cell population. Image quantification of fluorescence was performed using ImageJ software (Version 1.51, National Institutes of Health). The number of DAPI-positive cells expressing NESTIN, TUJ1, MAP2, GFAP (cytoplasmic staining), and SOX2 (nuclear staining) was quantified in 8–13 microscopic fields per sample.

Primary antibodies used in the immunofluorescence staining include: anti-NESTIN (1:200, Santa Cruz, Cat #sc-23927), anti-SOX2 (1:200, Abcam, ab97959), anti-SOX2 (1:200, Abcam, Cat #ab79351), anti-BrdU (1:300, Thermo Fisher Scientific, Cat #B35128), anti-BARHL2 (1:100, Proteintech, Cat #23976–1-AP) anti-IGF2BP2 (1:100, Proteintech, Cat #11601–1-AP), anti-IGF2BP3 (1:100, Santa Cruz, Cat #sc-390639), anti-FLAG (1:200, Abcam, Cat #ab1257), anti-TUJ1 (1:200, Abcam, Cat #ab78078), anti-MAP2 (1:200, Abcam, Cat #ab183830), anti-GFAP (1:200, Boster, Cat #PA1239).

BrdU and EdU labeling assays

BrdU powder (Sigma, #B5002) was dissolved in 10 mM PBS at 15 mg/ml and was incubated at 37°C for 15 minutes until it was completely dissolved. Mice were intraperitoneally injected with BrdU (50 mg/kg) at intervals of 24 hours for 5 days. Transcardiac perfusion was performed 3 hours after the last injection. The coronal cryosections of brains were obtained as described above for immunofluorescence staining. After three rinses in PBS, sections were incubated in 2N HCl for 40 minutes and blocked with PBS containing 5% BSA and 0.5% Triton X-100 for 1 hour (RT). The sections were incubated with primary antibody (anti-BrdU, Thermo Fisher Scientific, 1:300) and secondary antibody following the same method as above for immunofluorescence staining. All the sections were imaged using Zeiss LSM800 confocal laser scanning microscopy. The quantification of BrdU positive cells was performed using Zeiss ZEN 2.6 blue edition software. The count of BrdU and SOX2 double-positive cells was conducted across lateral, dorsolateral, and dorsal SVZ, while the count of BrdU and DCX double positive cells was conducted across the lateral and dorsolateral SVZ.

In the process of EdU (5-ethynyl-2′-deoxyuridine) labeling of cells, an equal volume of EdU solution from BeyoClick EdU assay kit (Beyotime, #C0071S) was added to the cell culture medium to label the cells for 2 hours except for the time-course labeling assay. The final concentration of EdU in the medium is 10 μM. After the labeling, cells were fixed with 4% paraformaldehyde solution for 10 mins at RT and washed with PBS three times. Cells were treated with 0.2% TritonX-100 for 5 mins at RT and washed with PBS three times. Staining for EdU was performed using the click buffer from BeyoClick EdU assay kit. Cell nuclei were stained with DAPI or Hoechst for 10 mins. The fluorescence signals of EdU in the cells were imaged using EVOS FL Cell Imaging System from Thermo Fisher Scientific. Images were captured to include a majority of the cells within each sample.

Image quantification of fluorescence was performed using ImageJ software. The number of cells showing the co-localization of EdU with DAPI or Hoechst fluorescence signals in the nuclei was quantified in a minimum of 10 microscopic fields per sample.

Cell death analysis by propidium iodide staining

Cell death analysis was performed using propidium iodide (PI) staining. Briefly, cells were incubated with a mixture of PI and Hoechst 33342 solution (Beyotime, #C1056) for 30 minutes at 4 °C in the dark. After staining, cells were washed with cold phosphate-buffered saline (PBS) to remove excess PI and Hoechst. The fluorescence signals of PI and Hoechst were detected using EVOS FL Cell Imaging System. Images were captured to cover most of the cells in each sample. Quantification of fluorescence intensity was performed using ImageJ software. The number of Hoechst-positive cells labeled with PI in nuclei was counted in 10 microscopic fields per sample.

Cell viability assay

Single cells were seeded in a 96-well plate for a high throughput assay of cell viability. The assay was performed with CellTiter-Lumi™ II Luminescent Assay Kit according to the manufacturer's instructions (Beyotime, #C0056M). The luminescent signals were measured in a plate reader with a luminometer system (Infinite 200 PRO, Tecan).

Quantitative real-time PCR

RNAs were converted into cDNAs through reverse transcription using TransScript Fly First-Strand cDNA Synthesis SuperMix (TransGen Biotech, Cat #AF301–02). Real-time qPCR analyses were performed using Hieff qPCR SYBR Green Master Mix (Yeasen Biotechnology Co. Ltd, Cat #11202ES08) on a QuantStudio 5 (Thermo Fisher Scientific). Data were collected by QuantStudio 5 Touchscreen Instrument Operating Software Version v1.5.1. The housekeeping gene GAPDH was used as endogenous control. Transcription levels of genes of interest and endogenous control were analyzed using the $2^{-\Delta\Delta CT}$ method[71].

scRNA-seq

The scRNA-seq library was prepared according to the manufacturer's instruction (10x Genomics single cell 3' v3 protocol). Briefly, the primary NSPCs were isolated from SVZ tissues pooled from six mice per group. The primary neurospheres were dissociated into single cells and counted using automated cell counter (Thermo Fisher Scientific). Cells displaying > 90% cell viability were resuspended in the master mix and loaded together with partitioning oil and gel beads into the chip to generate the gel bead-in-emulsion (GEM). The poly-A RNA from the cell lysate contained in every individual GEM was retrotranscribed to cDNA using an iIlumina R1 primer sequence, Unique Molecular Identifier (UMI) and the 10x Barcode. The pooled, barcoded cDNA was then purified with Silane DynaBeads, amplified by PCR and the appropriately-sized fragments were selected with SPRIselect reagent for subsequent library construction. During the library construction, the illumina R2 primer sequence, paired-end constructs with P5 and P7 sequences, and a sample index were added. Demultiplexing, barcode processing, gene counting, and aggregation were performed using Cell Ranger software v3.0.2 (10x Genomics). The Seurat R package (version 3) was

used for quality control and further data analysis. Quality control of the data was performed to filter cells by UMI (unique molecular identifier) counts (less than 2500 or over 7500) and percent of mitochondrial reads (> 20%). PCA was performed on the scaled data with default settings for linear dimensional reduction. Cells were clustered using Seurat's graph-based clustering approach with a resolution parameter of 0.5 and 20 principal components. UMAP was performed to visualize the data using the same principal components. Single-cell trajectory and pseudotime were analyzed using Monocle3 with reduction method of UMAP [26].

Bulk RNA-seq

Primary NSPCs were isolated from SVZ tissues pooled from six mice per group. Total RNA extraction of the primary NSPCs was performed using TRIzol Reagent following the manufacturer's instructions (Thermo Fisher Scientific). 1 mg of total RNA was used for rRNA depletion (rRNA depletion kit, MGI) and RNAseq library generation using MGIEasy RNA Library Prep Set (Item No. 1000006383). Total RNA-seq libraries were sequenced using the BGISEQ500 sequencer. For mRNA-seq, RNAs (> 200 nt) from primary NSPCs were purified using RNAeasy Animal RNA Isolation Kit with a spin column following the manufacturer's protocol (Beyotime, #R0028). 1 μg of RNA from each sample was used for mRNA enrichment using mRNA capture beads. After eluted from the beads, the purified mRNAs were subjected to library preparation using VAHTSTM mRNA-seq V3 Library Prep Kit for Illumina (Vazyme Biotech Co. Ltd, #NR611). mRNA-seq libraries were sequenced on Illumina NovaSeq 6000. Raw sequencing data from sequencer were converted into FASTQ files using bcl2fastq. In the data processing step, the RNA-seq reads were aligned to mm10 genome using TopHat or TopHat2 with default parameters. Aligned reads were converted to a sam format. Cuffdiff software was used to determine the transcript FPKM (Fragments Per Kilobase of transcript per Million mapped reads).

ChIP-seq

ChIP assay was performed as published[9]. Primary NSPCs were isolated from SVZ tissues pooled from six mice per group. Cells were fixed with 1% formaldehyde for 10 min and quenched with glycine solution for 20 min at room temperature. The fixed NSPCs were lysed in ChIP lysis buffer on ice. Chromatin was released during cell lysis and sonicated using an E220 focused-ultrasonicator (Covaris). Antibodies used in ChIP were: anti-H3K4me3 (1:300, Abcam, Cat #ab8580), anti-H3K27ac (1:300, Abcam, Cat #ab4927), anti-H3K27me3 (1:200, Abcam, Cat #ab192985). anti-KMT2D (1:200, Millipore, Cat #ABE1867), anti-RBBP5 (1:200, Cell Signaling, Cat #D316P), anti-WDR5 (1:200, Proteintech, Cat #15544–1-AP), anti-CBX3 (1:300, Millipore, Cat #05–690, clone 42s2).

ChIP-Seq libraries were prepared based on the protocol from the KAPA HyperPrep Kit (Roche) complemented with the NEXTflex DNA Barcodes (Bioo Scientific). All the libraries were sequenced using Illumina NextSeq 500. Raw sequencing data from sequencer were converted into FASTQ files using bcl2fastq. The ChIP-seq reads were aligned to the mm10 genome using Bowtie software with default settings. Only uniquely mapping reads with at most two mismatches were retained. The reads of repeated samples were merged in the BAM file for peak calling analysis. Peaks were called using MACS2[72] software with

default settings. Bedgraph (Bdg) files containing peak positions and signals were generated using MACS2.

ATAC-seq

Primary NSPCs were isolated from SVZ tissues pooled from six mice per group. The primary neurospheres were dissociated into single cells and cell viability measured using trypan blue staining. Approximately 2×10^4 NSPCs displaying > 90% cell viability were lysed on ice (lysis buffer: 10 mM Tris-HCl (pH 7.4), 10 mM NaCl, 3 mM $MgCl_2$, 0.1% Igepal CA-630). Cell nuclei were collected in a tube by centrifugation at 500 x g at 4°C and used for the tagmentation reaction in ATAC-Seq assay. ATAC-Seq libraries were prepared based on the protocol from the TruePrep DNA Library Prep Kit V2 for Illumina (Vazyme Biotech, Cat. #TD501). All the libraries were sequenced using Illumina HiSeq X Ten sequencer. Raw sequencing data from sequencer were converted into FASTQ files using bcl2fastq. The ATAC-seq reads were aligned to the mm10 genome using Burrows-Wheeler Aligner (BWA) with default settings. Only uniquely mapping reads with at most two mismatches were retained. The reads of repeated samples were merged for peak calling. All the reads were shifted +4 bp at the + strand and −5 bp at the - strand in the BAM file before peak calling. Peaks were called using MACS2 with --nomodel and --extsize 200 options. Bedgraph files containing peak positions and signals were generated using MACS2.

CUT&Tag assay

The CUT&Tag assay was performed using the Hyperactive Universal CUT&Tag Assay Kit for Illumina (Cat No. TD903, Vazyme Biotech Co. Ltd). Briefly, 10,000 cells were harvested and bound to Concanavalin A-coated beads. The cell-bead complexes were then incubated with a primary antibody against H3K4me3 (1:100, Abcam, Cat #ab8580) at room temperature for 1 hour, followed by an anti-rabbit secondary antibody (1:200) for 1 hour. Subsequently, the samples were treated with pA-Tn5 adapter mix for tagmentation at 37 ºC for 1 hour. After tagmentation, DNA was purified for PCR amplication. The resulting CUT&Tag libraries were sequenced using the Illumina NovaSeq 6000 platform. Raw sequencing data from sequencer were converted into FASTQ files using bcl2fastq. The CUT&Tag sequencing reads were aligned to the mm10 genome using Bowtie software with default settings. Only uniquely mapping reads with at most two mismatches were retained. Peaks were called using MACS2 software with default settings.

Immunoprecipitation and Western Blot

For the IP assay, cells were lysed in 1% TritonX-100 lysis buffer with protease inhibitor. Cell nuclei were collected by centrifugation at 4000 x g at 4°C and the pellet was lysed with 0.2% SDS lysis buffer. After centrifugation at 10000g at 4°C, the supernatant was collected for incubation with 1 μg antibody overnight at 4°C. The antigen-antibody complex was captured by Protein A or Protein G-conjugated Dynabeads (ThermoFisher Scientific). The IP products were eluted from the beads with SDS-PAGE sample loading buffer. Western blot analysis was performed as published[57]. Primary antibodies used were: anti-IGF2BP2 (1:1000, Proteintech, Cat #11601–1-AP), anti-KMT2D (1:1000, Millipore, Cat #ABE1867), anti-RBBP5 (1:1000, Cell Signaling, Cat #D316P), anti-WDR5 (1:1000, Proteintech, Cat #15544–1-AP), anti-CBX3 (1:1000, Millipore, Cat #05–690), anti-IgG (1:1000, Boster, Cat

#M04575–3), anti-TUBULIN (1:2000, Proteintech, Cat #66031–1-lg). The blot signals were measured with Bio-Rad ChemiDoc MP Imaging System, Image Lab 6.1 software.

LC/ tandem mass spectrometry (MS/MS) analysis of peptide.

The peptide mixture was analyzed by a home-made 30 cm-long pulled-tip analytical column (75 μm ID packed with ReproSil-Pur C18-AQ 1.9 μm resin, Dr. Maisch GmbH), the column was then placed in-line with an Easy-nLC 1200 nano HPLC (Thermo Fisher Scientific) for mass spectrometry analysis. The analytical column temperature was set at 55°C during the experiments. The mobile phase and elution gradient used for peptide separation were as follows: 0.1% formic acid in water as buffer A and 0.1% formic acid in 80% acetonitrile as buffer B, 0–1 min, 4%−8% B, 1–96 min, 8–35% B, 96–104 min, 35%−60% B, 104–105 min, 60%−100% B, 105–120 min, 100% B. The flow rate was set as 300 nl/min. Data-dependent tandem mass spectrometry (MS/MS) analysis was performed with a Q Exactive Orbitrap mass spectrometer (Thermo Fisher Scientific). Peptides eluted from the LC column were directly electrosprayed into the mass spectrometer with the application of a distal 2.5-kV spray voltage. A cycle of one full-scan MS spectrum (m/z 300–1800) was acquired followed by top 20 MS/MS events, sequentially generated on the first to the twentieth most intense ions selected from the full MS spectrum at a 30% normalized collision energy. The number of microscans was one for both MS and MS/MS scans and the maximum ion injection time was 50 and 100 ms, respectively. The dynamic exclusion settings used were as follows: charge exclusion, 1 and >7; exclude isotopes, on; and exclusion duration, 15 seconds. MS scan functions and LC solvent gradients were controlled by the Xcalibur data system (Thermo Fisher Scientific). The MS/MS data were analyzed in the UniProtKB Mus musculus database using Proteome Discoverer 2.1 (Thermo Fisher Scientific) or MaxQuant software package (version 1.6.10.43). To accurately estimate peptide probabilities and false discovery rates, we used a decoy database containing the reversed sequences of all the proteins appended to the target database. Both false discovery rates at peptide-spectrum match and protein levels were set to 0.01.

Statistics and Reproducibility

Statistical analyses with unpaired two-sided Student's *t-test* were performed using GraphPad Prism software and mentioned in the Figure captions. The statistical data were presented as mean ± SD. "n" represented the number of experimental objects including animals and cells or the number of independent experiments and was also mentioned in the Figure captions. A significant overlap of gene number was determined by the hypergeometric test. No statistical methods were used to pre-determine sample sizes but our sample sizes are similar to those reported in previous publications[6, 9, 66]. No animal data or data points were excluded from the analyses. Young and aged mice were randomly assigned to their respective experimental groups. Cell images were randomly captured for analysis using the microscope software. Investigators were blinded to the age of the cells when preparing sequencing libraries, running the sequencers, and raw sequencing data processing. Blinding for bioinformatics analysis of sequencing data was not applicable due to the automated and objective nature of the analysis, and the need for integrated analysis across varied NGS datasets. During data collection for immunofluorescence staining experiments, group allocation was blinded. Data analysis of immunofluorescence staining was not blinded due to the need for interpretation

of the data. Data collection and analysis in other experiments were not performed blind to the conditions of the experiments.

Extended Data

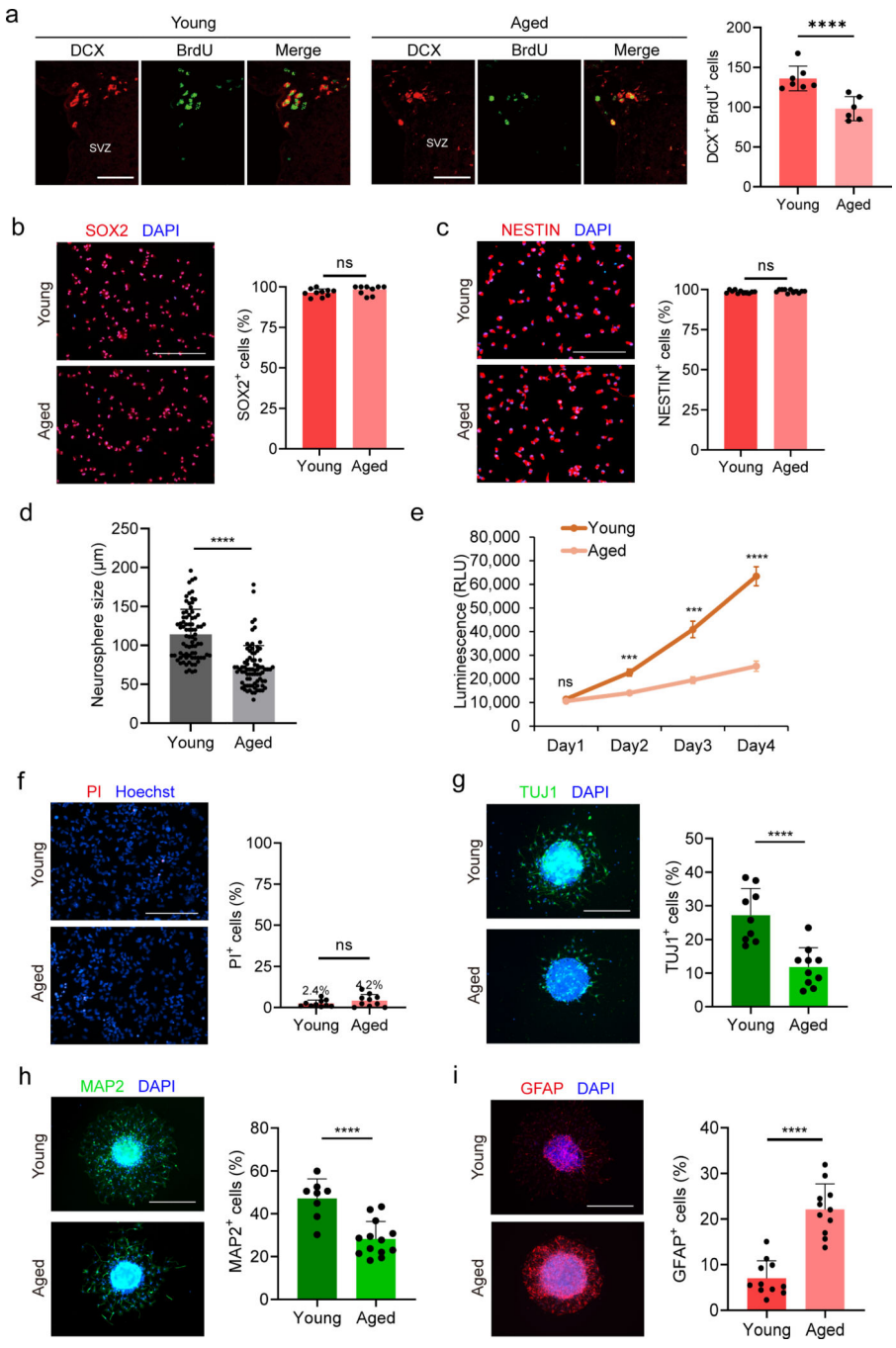

Extended Data Fig. 1: Aged NSPCs exhibit reduced potential for differentiating into neurons compared to young NSPCs.

a, Confocal microscopy images showing immunofluorescence co-labeling of DCX and BrdU in the coronal SVZ sections from young and aged mice. Scale bar, 40 μm. The

quantification of DCX and BrdU double-positive cells was performed in both the lateral and dorsolateral SVZ for each section. A total of four sections per mouse, spaced at 120 μm intervals along the rostrocaudal axis of the SVZ, were used for cell counting. Seven mice per young group. Six mice per aged group. The average number of DCX and BrdU double-positive cells per group was plotted in the chart on the right panel. $P = 0.0009$. **** $P < 0.001$. **b,** Immunofluorescence labeling of SOX2 in NSPCs isolated from the young and aged SVZ, respectively. Primary NSPC-derived neurospheres were dissociated into single cells for staining. Nuclei were stained with DAPI. Scale bar, 200 μm. Quantification data were plotted, showing the percentage of SOX2-positive cells among DAPI-positive cells counted from 10 microscopic fields per age group. ns: not significant. **c,** Immunofluorescence labeling of NESTIN in NSPCs isolated from the young and aged SVZ, respectively. The staining and quantification methods used are identical to those described in (b). **d,** The size of primary NSPC-derived neurospheres in young and aged groups. Neurospheres were imaged after 6 days of culture, and their diameters were measured through ImageJ software. n = 80. $P = 3.05E\text{-}15$. **** $P < 0.001$. **e,** Luminescent cell viability analysis of young and aged NSPCs cultured from Day 1 to Day 4. n = 3 independent experiments. Day1: $P = 0.2436$, Day2: $P = 0.0012$, Day3: $P = 0.0013$, Day4: $P = 0.0003$. *** $P < 0.005$. **** $P < 0.001$. ns: not significant. **f,** Cell death analysis by propidium iodide (PI) staining. Scale bar, 200 μm. Quantification data were plotted, showing the percentage of PI-positive cells among Hoechst-positive cells counted from 10 microscopic fields per age group. **g,** Neural differentiation starting from NSPC-derived neurosphere as neurite outgrows. After 2 days of differentiation, cells were fixed and subjected to immunofluorescence labeling of neuron marker TUJ1. The number of TUJ1+ differentiated cells with neurites that migrated away from the neurosphere was counted. Scale bar, 200 μm. Data were plotted with the percentage of TUJ1 versus DAPI-positive cells with neurites in each neurosphere differentiation. n = 10. $P = 6.71E\text{-}05$. **h,** Immunofluorescence labeling of neuron marker MAP2 four days post-differentiation. The number of MAP2+ differentiated cells that migrated away from the neurosphere was counted. Scale bar, 200 μm. n = 8 in young group. n = 13 in aged group. $P = 4.83E\text{-}06$. **i,** Immunofluorescence labeling of astrocyte marker GFAP four days post-differentiation. The number of GFAP+ differentiated cells that migrated away from the neurosphere was counted. Scale bar, 200 μm. Data were plotted with the percentage of GFAP-positive cells with astrocytic extensions versus DAPI-positive cells in each neurosphere differentiation. n = 13 per group. Data analysis for g-i: $P = 3.99E\text{-}07$. *** $P < 0.005$. **** $P < 0.001$. Error bars are mean ± SD in all graphs. Two-sided Student's *t-test* for statistical analysis in all graphs.

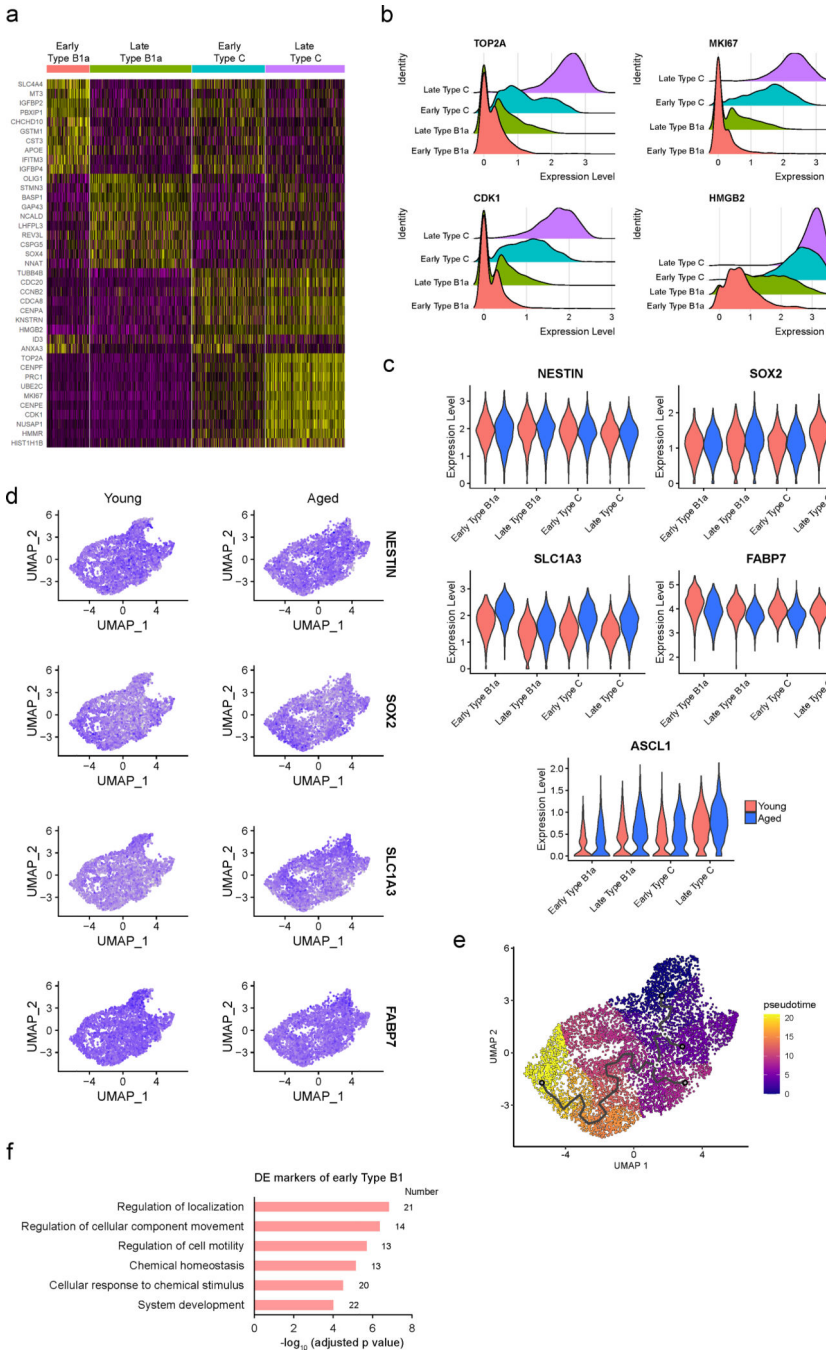

Extended Data Fig. 2: Identification of NSPC activation states and lineage specificity through single-cell transcriptome.

a, Heatmap of top 10 differentially expressed marker genes in 4 clusters of NSPCs. Analysis was performed using merged scRNA-seq datasets of young and aged NSPCs. **b,** Ridgeline plots of merged scRNA-seq datasets of young and aged NSPCs, showing expression changes of activation markers from early type B1a cells to late type C cells. **c,** Violin plots showing the similar expression levels of NSPC lineage markers among 4 clusters between young and aged NSPCs. **d,** UMAP plots of NSPC lineage markers in young and aged NSPCs.

e, Single-cell pseudotime analysis using Monocle3 shows dynamic transition of NSPC activation states along the trajectory. NSPCs with larger pseudotime values exhibit higher activity in proliferation. **f,** Gene ontology analysis of the DE markers of early type B1a cells. The gene number of each GO category is showed on the right side of the bar chart.

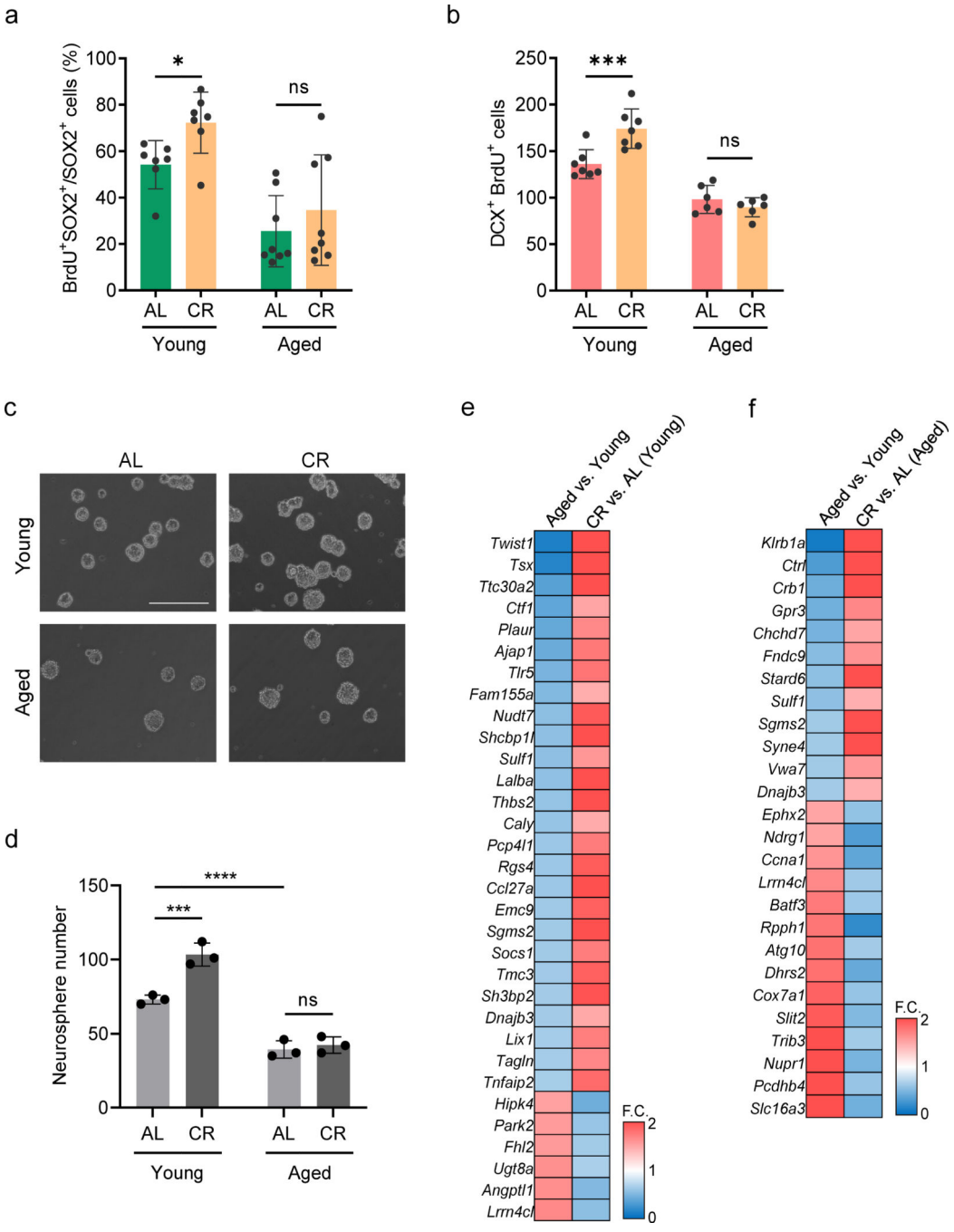

Extended Data Fig. 3: Transcriptional reversal of age-dependent genes is associated with the functional improvement of NSPCs in mice subjected to calorie restriction.

a, Percentage of BrdU and SOX2 double-positive versus SOX2-positive cells in the brain SVZs of young and aged mice subjected to AL and CR treatments. Seven mice per young

group; eight mice per aged group. Twelve sections per mouse. Error bars are mean ± SD. Unpaired two-sided Student's *t-test*. Young: $P = 0.0146$, Aged: $P = 0.3789$. * $P < 0.05$. ns: not significant. **b,** Quantification of DCX and BrdU double-positive cells in both the lateral and dorsolateral SVZ of young and aged mice subjected to AL and CR treatments. A total of four sections per mouse, spaced at 120 μm intervals along the rostrocaudal axis of the SVZ, were used for cell counting. Seven mice per young group. Six mice per aged group. Error bars are mean ± SD. Unpaired two-sided Student's *t-test*. Young: $P = 0.0024$, Aged: $P = 0.28$. *** $P < 0.005$. ns: not significant. **c,** Representative images of neurospheres formed by primary NSPCs isolated from the SVZ of mice subjected to ad libitum (AL) feeding or calorie restriction (CR) within each age group. Scale bar, 1000 μm. The SVZ tissues were pooled from five mice per group. **d,** Number of neurospheres was quantified across four groups of mice as in (a). n = 3 independent cultures. Six microscopic fields were imaged from each culture replicate for cell counting. Error bars are mean ± SD. Unpaired two-sided Student's *t-test*. Young_AL vs. Young_CR: $P = 0.0032$, Young_AL vs. Aged_AL: $P = 0.0009$, Aged_AL vs. Aged_CR: $P = 0.5534$. *** $P < 0.005$. **** $P < 0.001$. ns: not significant. **e, f,** Heatmap showing the fold change in transcriptional levels of age-dependent genes (Aged vs. Young, FC > 1.5) and their transcriptional reversal in young (c) or aged (d) mice subjected to calorie restriction (CR vs. AL, FC > 1.5).

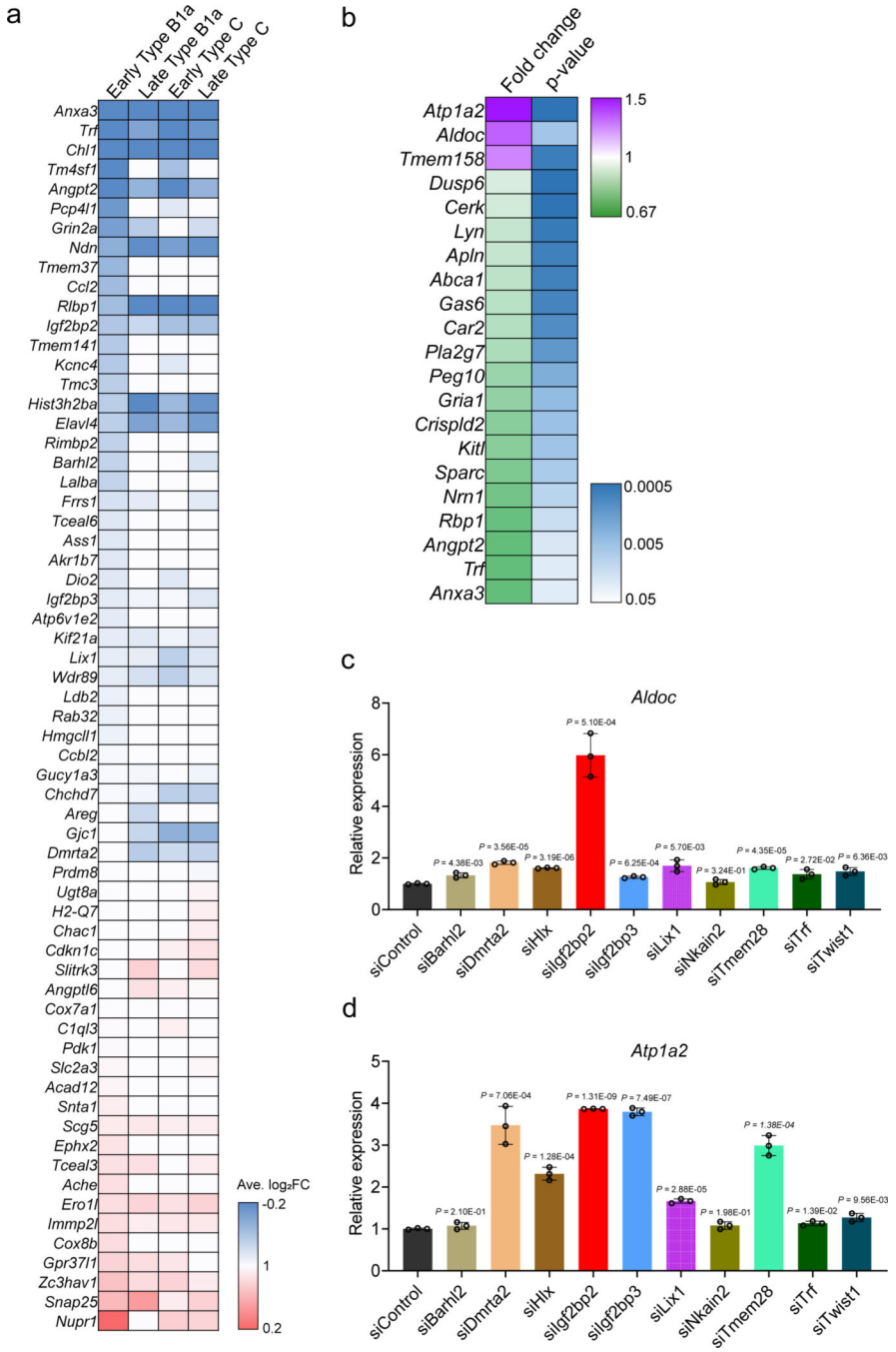

Extended Data Fig. 4: Downregulation of age-dependent gene upregulates NSC quiescence markers.

a, Heatmap showing scRNA-seq differential expression analysis of the age-dependent genes identified in bulk RNA-seq in each NSPC cluster. Data are the average log2 fold change of expression. **b,** Heatmap showing bulk RNA-seq differential expression analysis of DE genes detected in early type B1a cells as in Figure 1j. Fold change of RNA level (Aged_FPKM vs. Young_FPKM) and p-value were plotted. **c, d,** Quantitative real-time PCR analysis of relative expression (siRNA group vs. siControl group) of *Aldoc* and *Atp1a2* in young

NSPCs 48 hours after siRNA transfection. n = 3 independent assays. Error bars are mean ± SD. Unpaired two-sided Student's *t-test*.

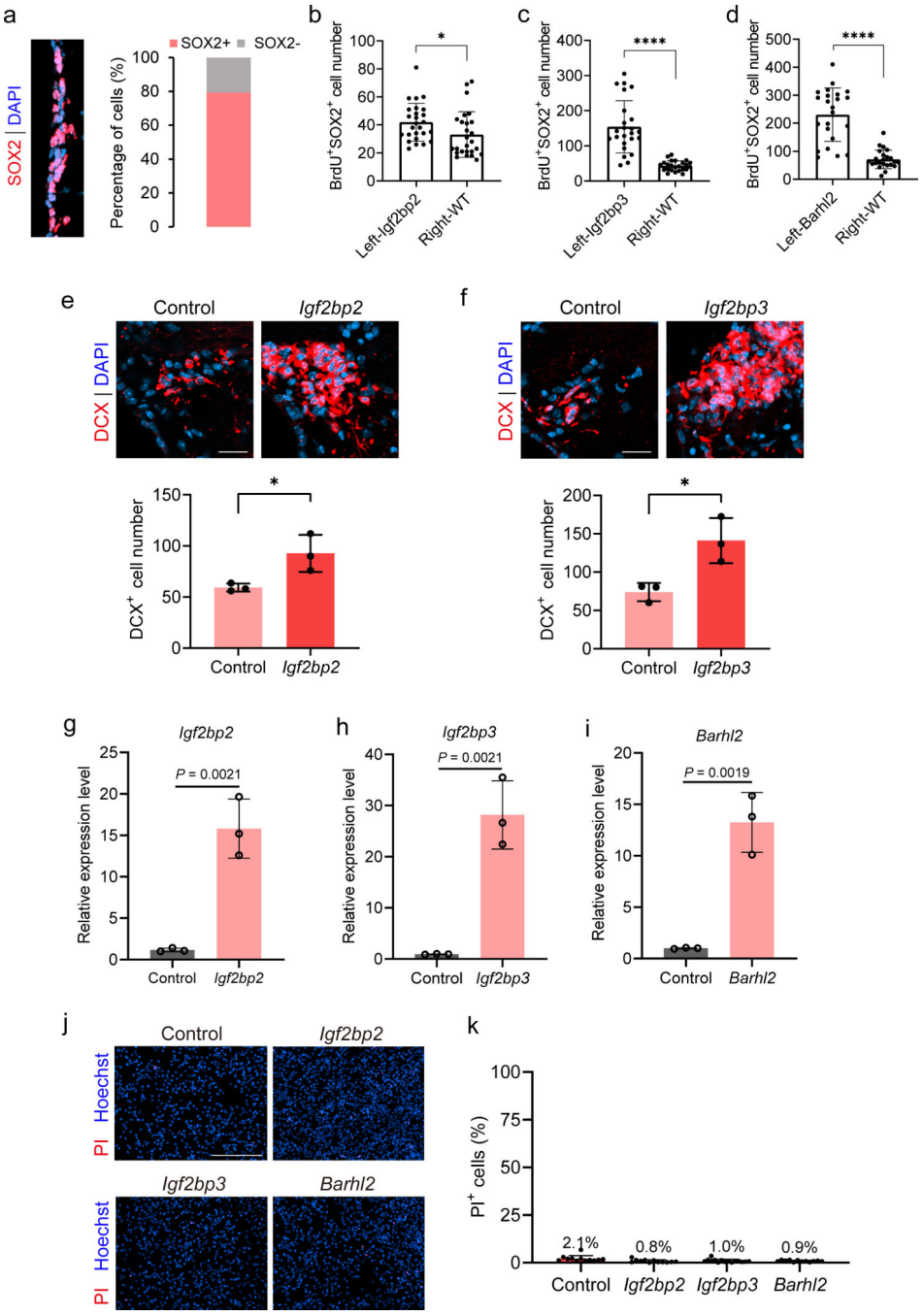

Extended Data Fig. 5: The rejuvenating effects of age-dependent genes on aged NSPCs.

a, Quantification of SOX2-positive cells in the SVZ. The average percentage of SOX2+/DAPI+ cells was plotted based on data from three aged wild-type mice. A total of eight sections per mouse, spaced at 120 μm intervals along the rostrocaudal axis of the SVZ, were used for cell counting. Cells were quantified within the lateral and dorsolateral

SVZ in each section. **b-d,** Quantification of BrdU+SOX2+ NSPCs in the left (*Igf2bp2*, *Igf2bp3*, and *Barhl2* overexpression) and right (wild-type) sides of the SVZ. The adenovirus encoding these genes were injected in the left side of SVZ of aged mice, respectively. BrdU labeling was performed two weeks after the gene transduction. BrdU+SOX2+ NSPCs were quantified at both sides of the lateral and dorsolateral SVZ in each section. Seven sections per mouse. Three mice per group. Unpaired two-sided Student's *t-test*. (b): $P = 0.0396$, (c): $P = 5.05E-09$, (d): $P = 1.39E-08$. * $P < 0.05$. **** $P < 0.001$. **e, f,** Overexpression of *Igf2bp2* and *Igf2bp3* increases the number of DCX-positive cells in the SVZ of aged mice. Control mice were injected with control adenovirus without expressing these genes. Confocal microscopy images showing immunofluorescence co-labeling of DCX and DAPI in the SVZ. Scale bar, 20 μm. DCX-positive cells were quantified at the injection site within the lateral and dorsolateral SVZ in each section. A total of six sections per mouse, spaced at 120 μm intervals along the rostrocaudal axis of the SVZ, were used for cell counting. Three mice per group. The average number of DCX-positive cells per group was plotted blow the images. Unpaired two-sided Student's *t-test*. (e): $P = 0.0355$, (f): $P = 0.0216$. * $P < 0.05$. **g-i,** Quantitative real-time PCR analysis of relative expression of *Igf2bp2*, *Igf2bp3*, and *Barhl2* 40 hours after the adenovirus-mediated transduction of the respective genes in primary aged NSPCs. The control group was transduced with control adenovirus without expressing these genes. n = 3 independent assays. Unpaired two-sided Student's *t-test*. **j,** Cell death analysis by propidium iodide (PI) staining in primary aged NSPCs transduced with the genes of *Igf2bp2*, *Igf2bp3*, and *Barhl2*. NSPC-formed neurospheres were dissociated into single cells for staining 48 hours following adenovirus-mediated transduction of the respective genes. Scale bar, 200 μm. **k,** Quantification data of PI staining shows the percentage of PI-positive cells among Hoechst-positive cells, which were counted from 10 microscopic fields per group. Error bars are mean ± SD for b-k.

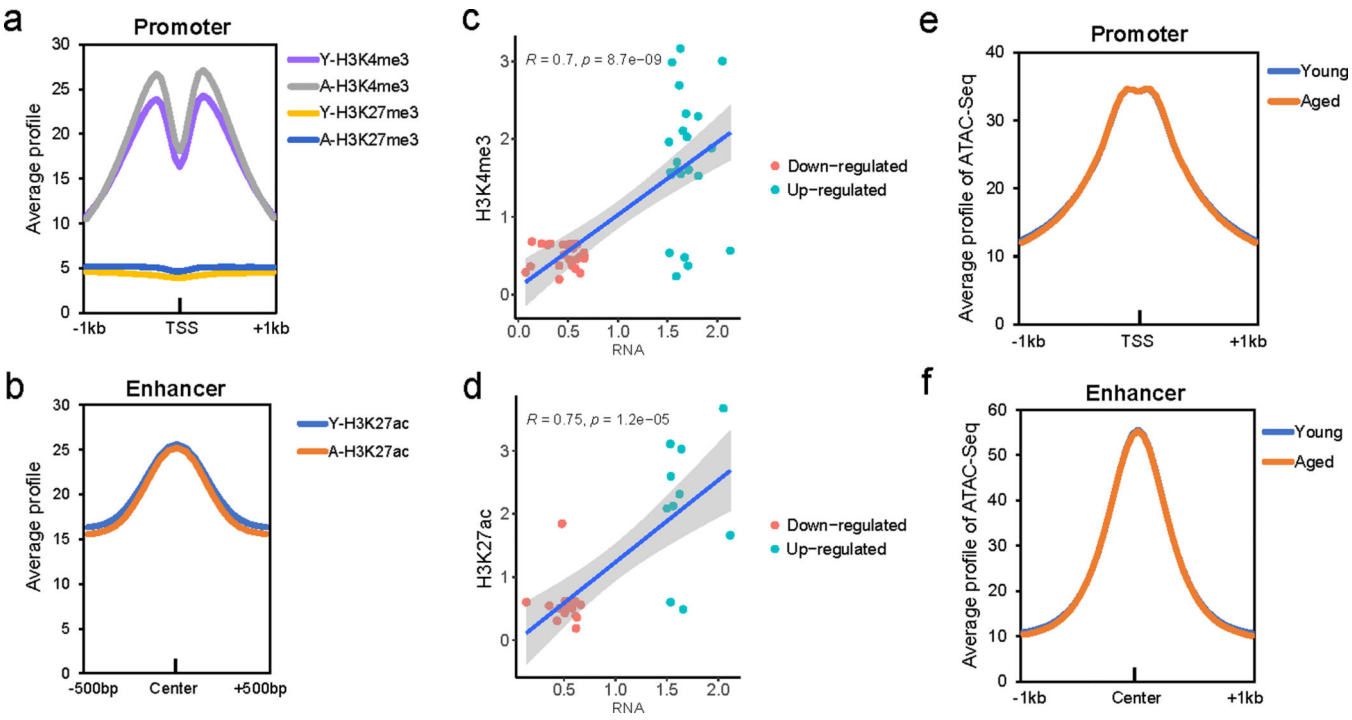

Extended Data Fig. 6: Changes in average profiles of histone marks and ATAC-seq signals at promoters and enhancers in aging NSPCs.

a, Average profile of H3K4me3 and H3K27me3 at the promoters of all genes spanning TSSs in young and aged NSPCs (Two-sided Wilcoxon rank sum test, H3K4me3 data p-value = 0.2209, H3K27me3 data p-value = 6.69E-15). **b,** Average profile of H3K27ac signals spanning the center of enhancers of all genes in young and aged NSPCs (Two-sided Wilcoxon rank sum test, H3K27ac data p-value = 0.2684). **c,** Pearson correlation analysis of fold changes of RNA levels and promoter H3K4me3 signals of age-dependent genes. 95% confidence interval. **d,** Pearson correlation analysis of fold changes of RNA levels and enhancer H3K27ac signals of age-dependent genes. 95% confidence interval. **e, f,** Average profiles of ATAC- seq at promoters and enhancers of all genes show no genome-wide changes of chromatin accessibility across the regulatory elements during NSPC aging (Two-sided Wilcoxon rank sum test, promoter profile p-value = 0.9261, enhancer profile p-value = 0.6969).

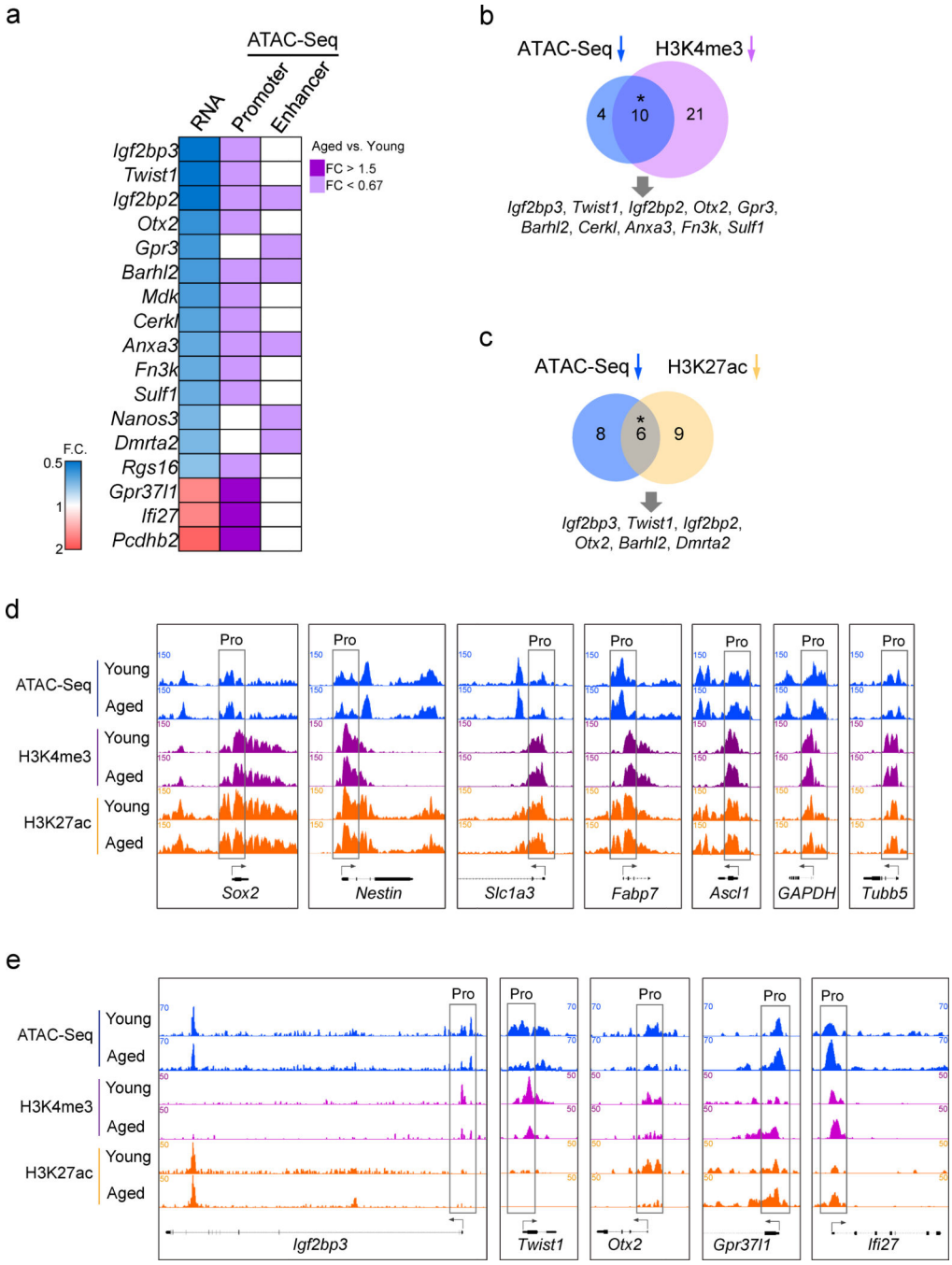

Extended Data Fig. 7: Histone modifications are associated with chromatin accessibility at the promoters of age-dependent genes in aging NSPCs.

a, Heatmap shows fold change (Aged vs. Young) of RNA levels of age-dependent genes and the average signals of ATAC-seq at their regulatory elements. **b,** Venn diagrams show the overlap of age-dependent genes that have decreased levels of chromatin accessibility and H3K4me3 at the promoters during NSPC aging. Two-sided Hypergeometric test for significant overlap analysis, * p-value = 5.602e-26. **c,** Venn diagrams show the overlap of age- dependent genes that have decreased levels of chromatin accessibility and H3K27ac

signals at the enhancers during NSPC aging. Two-sided Hypergeometric test, * p-value = 3.618e-16. **d,** Browser tracks of ATAC-seq and ChIP-seq show a similar level of signals at the promoters of NSPC lineage markers and housekeeping genes between the young and aged groups. **e,** Browser tracks of 3 age-dependent down-regulated genes (*Igf2bp3*, *Twist1*, and *Otx2*) and 2 up-regulated genes (*Gpr37l1* and *Ifi27*) that have changes of ATAC-seq signals and histone modifications at the promoters during NSPC aging.

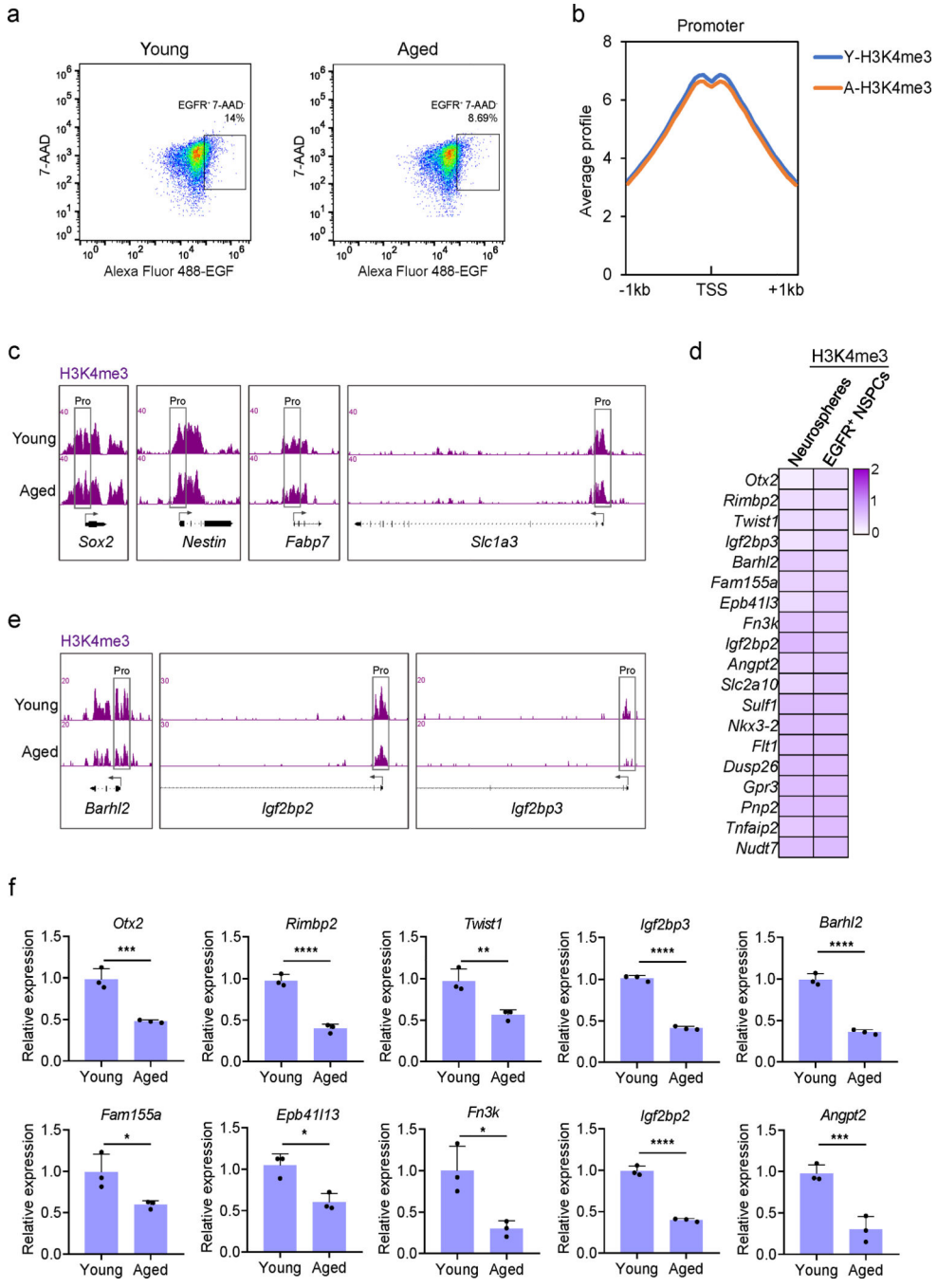

Extended Data Fig. 8: Age-related changes in histone modifications and transcription in aging EGFR$^+$ NSPCs.

a, FACS plots of the isolation of EGFR-positive and 7-AAD negative NSPCs from the SVZ of young and aged mice. **b,** Average profile of H3K4me3 at the promoters of all genes spanning TSSs in young and aged $EGFR^+$ NSPCs (Two-sided Wilcoxon rank sum test, H3K4me3 data p-value = 0.5428). **c,** Browser tracks of CUT&Tag signals of H3K4me3 at the promoters of NSPC lineage markers in young and aged $EGFR^+$ NSPCs. **d,** Heatmap showing the fold change of average CUT&Tag signals of H3K4me3 at each promoter of age-dependent genes in aged NSPC-derived neurospheres or $EGFR^+$ NSPCs compared to their young counterparts (Aged vs. Young, FC > 1.5). **e,** Browser tracks of CUT&Tag signals at the promoters of *Barhl2*, *Igf2bp2*, and *Igf2bp3*. **f,** Real-time qPCR analysis of relative expression of genes in aged versus young $EGFR^+$ NSPCs. Error bars are mean ± SD. n = 3 independent assays. Two-sided Student's *t*-tests. *Otx2*: $P = 0.0021$, *Rimbp2*: $P = 0.0003$, *Twist1*: $P = 0.0099$, *Igf2bp3*: $P = 7.77E\text{-}06$, *Barhl2*: $P = 0.0001$, *Fam155a*: $P = 0.0382$, *Epb41l13*: $P = 0.0109$, *Fn3k*: $P = 0.0174$, *Igf2bp2*: $P = 7.57E\text{-}05$, *Angpt2*: $P = 0.0035$. * $P < 0.05$. ** $P < 0.01$. *** $P < 0.005$. **** $P < 0.001$.

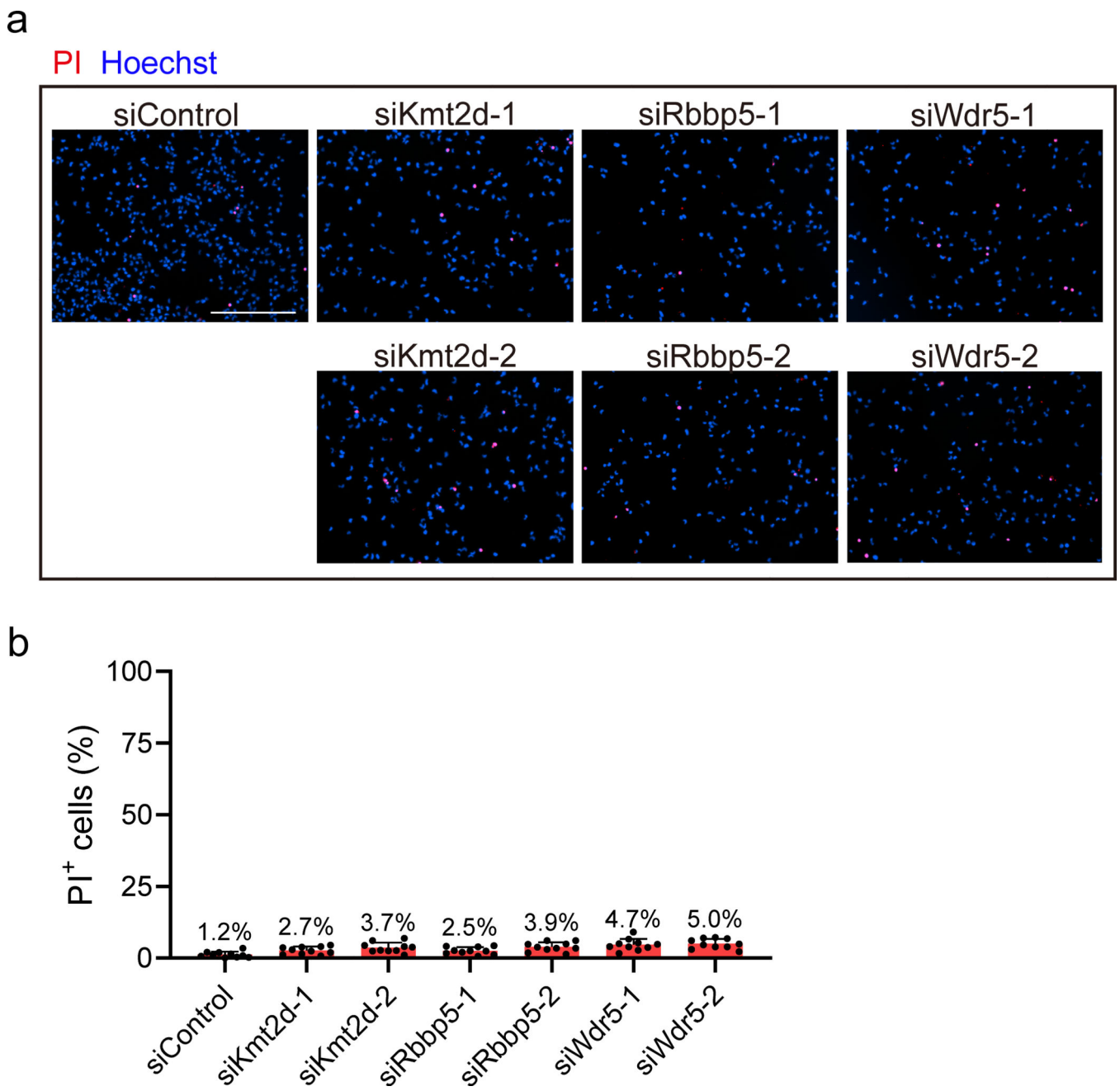

Extended Data Fig. 9: Cell death analysis by propidium iodide (PI) staining in NSPCs following knockdown of MLL complex subunits.

a, Representative immunofluorescence images showing PI staining in siRNA-transfected young NSPCs. NSPC-derived neurospheres were dissociated into single cells for PI staining 48 hours post-transfection of siRNAs. Hoechst (blue) staining visualizes the nuclei. Scale bar, 200 μm. **b,** Quantification of PI staining in siRNA-transfected young NSPCs, displaying the percentage of PI-positive cells among Hoechst-positive cells. The quantification was performed by counting from 10 microscopic fields per group. Error bars are mean ± SD.

a

KMT2D IP-MS

Name	MW [kDa]	Accession	Peptides
KMT2D	599.9	Q6PDK2	113
ASH2L	68.2	Q91X20	23
RBBP5	59.1	Q8BX09	15
WDR5	36.6	P61965	10
DPY30	11.2	Q99LT0	3
CBX3	20.8	P23198	9

b

CBX3 IP-MS

	Name	MW [kDa]	Accession	Peptides
	CBX3	20.8	P23198	15
MLL complex	KMT2D	599.9	Q6PDK2	123
	ASH2L	68.2	Q91X20	26
	RBBP5	59.1	Q8BX09	19
	WDR5	36.6	P61965	11
	DPY30	11.2	Q99LT0	6
	EHMT1	141.9	Q5DW34	11
	EHMT2	138	Q9Z148	11

CBX3 MLL complex Avg. peptides=37 HMTase Avg. peptides=11

c

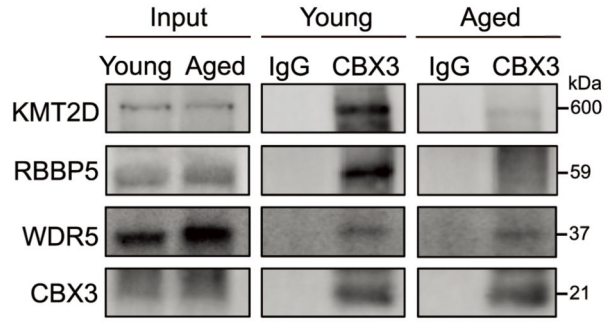

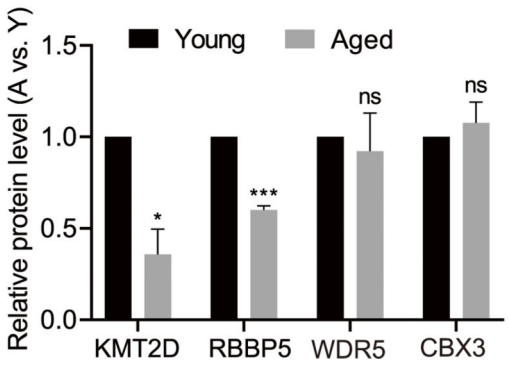

Extended Data Fig. 10: Interaction between MLL complex and Cbx3 in aging NSPCs.

a, Mass spectrometry peptide counts (number of unique peptides) of MLL complex components identified in KMT2D immunoprecipitation product from young NSPC nuclear extract. **b,** Mass spectrometry peptide counts (number of unique peptides) of proteins identified in CBX3 immunoprecipitation product from young NSPC nuclear extract. **c,** Western blot analysis of endogenous MLL complex components in CBX3 and IgG immunoprecipitation products from the young and aged NSPC nuclear extracts. Bar charts show the relative levels of the indicated proteins in aged versus young IP groups analyzed by Image J software. Error bars are mean ± SD. n = 2 independent experiments, Unpaired two-sided Student's *t*-tests. KMT2D: $P = 0.0222$, RBBP5: $P = 0.0015$, WDR5: $P = 0.6499$, CBX3: $P = 0.4363$. * $P < 0.05$. *** $P < 0.005$. ns: not significant.

Supplementary Material

Refer to Web version on PubMed Central for supplementary material.

Acknowledgements

We thank Dr. Danian Qin, Qiang Shan, and Ziqi Cai (Shantou University Medical College) for their technical support of stereotactic injection of mice. Thanks to Bo Wang for technical support of animal studies. Thanks to Xialei Hu for technical support of NSPC isolation from the SVZ. Thanks to Dr. Trent Su (University of California at Los Angeles, UCLA) for bioinformatic support. Thanks to Dr. Chao Peng and Yue Yin of the Mass Spectrometry System at the National Facility for Protein Science in Shanghai (NFPS), Shanghai Advanced Research Institute, Chinese Academy of Science, for data collection and analysis. This work was supported by National Natural

Science Foundation of China (grant number 81671396, C.H.), Natural Science Foundation of Guangdong Province (grant number 2017A030313780, C.H.), and NIH grant R01 (grant number GM074701, M.C.).

Data availability

All the sequencing data have been submitted to Gene Expression Omnibus (GEO) and are publicly available as of the date of publication. The accession number for the sequencing data is GSE212725. UniProtKB Mus musculus database was used for mass spectrometry data analysis (database link: https://www.uniprot.org/taxonomy/10090). All other data supporting the findings of this manuscript will be available from the corresponding author upon request.

References

1. Oh J, Lee YD & Wagers AJ Stem cell aging: mechanisms, regulators and therapeutic opportunities. Nat Med 20, 870–880 (2014). [PubMed: 25100532]
2. Doetsch F, Caille I, Lim DA, Garcia-Verdugo JM & Alvarez-Buylla A. Subventricular zone astrocytes are neural stem cells in the adult mammalian brain. Cell 97, 703–716 (1999). [PubMed: 10380923]
3. Lim DA & Alvarez-Buylla A. The Adult Ventricular-Subventricular Zone (V-SVZ) and Olfactory Bulb (OB) Neurogenesis. Cold Spring Harb Perspect Biol 8 (2016).
4. Bondolfi L, Ermini F, Long JM, Ingram DK & Jucker M. Impact of age and caloric restriction on neurogenesis in the dentate gyrus of C57BL/6 mice. Neurobiol Aging 25, 333–340 (2004). [PubMed: 15123339]
5. Maslov AY, Barone TA, Plunkett RJ & Pruitt SC Neural stem cell detection, characterization, and age-related changes in the subventricular zone of mice. J Neurosci 24, 1726–1733 (2004). [PubMed: 14973255]
6. Molofsky AV et al. Increasing p16INK4a expression decreases forebrain progenitors and neurogenesis during ageing. Nature 443, 448–452 (2006). [PubMed: 16957738]
7. Tobin MK et al. Human Hippocampal Neurogenesis Persists in Aged Adults and Alzheimer's Disease Patients. Cell Stem Cell 24, 974–982 e973 (2019). [PubMed: 31130513]
8. Liu P. et al. Histone deacetylation promotes mouse neural induction by restricting Nodal-dependent mesendoderm fate. Nat Commun 6, 6830 (2015). [PubMed: 25904100]
9. Huang C. et al. Cbx3 maintains lineage specificity during neural differentiation. Genes Dev 31, 241–246 (2017). [PubMed: 28270516]
10. Qiao Y, Yang X. & Jing N. Epigenetic regulation of early neural fate commitment. Cell Mol Life Sci 73, 1399–1411 (2016). [PubMed: 26801220]
11. Pearson CA et al. Foxp1 Regulates Neural Stem Cell Self-Renewal and Bias Toward Deep Layer Cortical Fates. Cell Rep 30, 1964–1981 e1963 (2020). [PubMed: 32049024]
12. Zhang K. et al. Distinct functions of BMP4 during different stages of mouse ES cell neural commitment. Development 137, 2095–2105 (2010). [PubMed: 20504958]
13. Hirabayashi Y. & Gotoh Y. Epigenetic control of neural precursor cell fate during development. Nat Rev Neurosci 11, 377–388 (2010). [PubMed: 20485363]
14. Kalamakis G. et al. Quiescence Modulates Stem Cell Maintenance and Regenerative Capacity in the Aging Brain. Cell 176, 1407–1419 e1414 (2019). [PubMed: 30827680]
15. Lupo G. et al. Molecular profiling of aged neural progenitors identifies Dbx2 as a candidate regulator of age-associated neurogenic decline. Aging Cell 17, e12745 (2018). [PubMed: 29504228]
16. Yang JH et al. Loss of epigenetic information as a cause of mammalian aging. Cell 186, 305–326 e327 (2023). [PubMed: 36638792]

17. Ellis P. et al. SOX2, a persistent marker for multipotential neural stem cells derived from embryonic stem cells, the embryo or the adult. Dev Neurosci 26, 148–165 (2004). [PubMed: 15711057]
18. Ferri AL et al. Sox2 deficiency causes neurodegeneration and impaired neurogenesis in the adult mouse brain. Development 131, 3805–3819 (2004). [PubMed: 15240551]
19. Suh H. et al. In vivo fate analysis reveals the multipotent and self-renewal capacities of Sox2+ neural stem cells in the adult hippocampus. Cell Stem Cell 1, 515–528 (2007). [PubMed: 18371391]
20. Brazel CY et al. Sox2 expression defines a heterogeneous population of neurosphere-forming cells in the adult murine brain. Aging Cell 4, 197–207 (2005). [PubMed: 16026334]
21. Stuart T. et al. Comprehensive Integration of Single-Cell Data. Cell 177, 1888–1902 e1821 (2019). [PubMed: 31178118]
22. Mich JK et al. Prospective identification of functionally distinct stem cells and neurosphere-initiating cells in adult mouse forebrain. Elife 3, e02669 (2014). [PubMed: 24843006]
23. Giachino C. et al. Molecular diversity subdivides the adult forebrain neural stem cell population. Stem Cells 32, 70–84 (2014). [PubMed: 23964022]
24. Kim EJ, Leung CT, Reed RR & Johnson JE In vivo analysis of Ascl1 defined progenitors reveals distinct developmental dynamics during adult neurogenesis and gliogenesis. J Neurosci 27, 12764–12774 (2007). [PubMed: 18032648]
25. Ponti G. et al. Cell cycle and lineage progression of neural progenitors in the ventricular-subventricular zones of adult mice. Proc Natl Acad Sci U S A 110, E1045–1054 (2013). [PubMed: 23431204]
26. Cao J. et al. The single-cell transcriptional landscape of mammalian organogenesis. Nature 566, 496–502 (2019). [PubMed: 30787437]
27. Shin J. et al. Single-Cell RNA-Seq with Waterfall Reveals Molecular Cascades underlying Adult Neurogenesis. Cell Stem Cell 17, 360–372 (2015). [PubMed: 26299571]
28. Basak O. et al. Troy+ brain stem cells cycle through quiescence and regulate their number by sensing niche occupancy. Proc Natl Acad Sci U S A 115, E610–E619 (2018). [PubMed: 29311336]
29. Adusumilli VS et al. ROS Dynamics Delineate Functional States of Hippocampal Neural Stem Cells and Link to Their Activity-Dependent Exit from Quiescence. Cell Stem Cell 28, 300–314 e306 (2021). [PubMed: 33275875]
30. Naeve GS et al. Neuritin: a gene induced by neural activity and neurotrophins that promotes neuritogenesis. Proc Natl Acad Sci U S A 94, 2648–2653 (1997). [PubMed: 9122250]
31. Erickson RI, Paucar AA, Jackson RL, Visnyei K. & Kornblum H. Roles of insulin and transferrin in neural progenitor survival and proliferation. J Neurosci Res 86, 1884–1894 (2008). [PubMed: 18293414]
32. Boschian C. et al. Impaired Neuronal Differentiation of Neural Stem Cells Lacking the Engrailed-2 Gene. Neuroscience 386, 137–149 (2018). [PubMed: 29964155]
33. Khodosevich K. et al. Connexin45 modulates the proliferation of transit-amplifying precursor cells in the mouse subventricular zone. Proc Natl Acad Sci U S A 109, 20107–20112 (2012). [PubMed: 23169657]
34. Young FI et al. The doublesex-related Dmrta2 safeguards neural progenitor maintenance involving transcriptional regulation of Hes1. Proc Natl Acad Sci U S A 114, E5599–E5607 (2017). [PubMed: 28655839]
35. Lim DA et al. Chromatin remodelling factor Mll1 is essential for neurogenesis from postnatal neural stem cells. Nature 458, 529–533 (2009). [PubMed: 19212323]
36. Apple DM, Mahesula S, Fonseca RS, Zhu C. & Kokovay E. Calorie restriction protects neural stem cells from age-related deficits in the subventricular zone. Aging (Albany NY) 11, 115–126 (2019). [PubMed: 30622221]
37. Parish EV, Mason JO & Price DJ Expression of Barhl2 and its relationship with Pax6 expression in the forebrain of the mouse embryo. BMC Neurosci 17, 76 (2016). [PubMed: 27887593]

38. Bates MD, Dunagan DT, Welch LC, Kaul A. & Harvey RP The Hlx homeobox transcription factor is required early in enteric nervous system development. BMC Dev Biol 6, 33 (2006). [PubMed: 16854219]
39. Li Z. et al. An HMGA2-IGF2BP2 axis regulates myoblast proliferation and myogenesis. Dev Cell 23, 1176–1188 (2012). [PubMed: 23177649]
40. Mori H. et al. Expression of mouse igf2 mRNA-binding protein 3 and its implications for the developing central nervous system. J Neurosci Res 64, 132–143 (2001). [PubMed: 11288142]
41. Leitner DF & Connor JR Functional roles of transferrin in the brain. Biochim Biophys Acta 1820, 393–402 (2012). [PubMed: 22138408]
42. Fan X. et al. TWIST1 and chromatin regulatory proteins interact to guide neural crest cell differentiation. Elife 10 (2021).
43. McKey J, Martire D, de Santa Barbara P. & Faure S. LIX1 regulates YAP1 activity and controls the proliferation and differentiation of stomach mesenchymal progenitors. BMC Biol 14, 34 (2016). [PubMed: 27125505]
44. Chua HC, Wulf M, Weidling C, Rasmussen LP & Pless SA The NALCN channel complex is voltage sensitive and directly modulated by extracellular calcium. Sci Adv 6, eaaz3154 (2020).
45. Preitner N, Quan J, Li X, Nielsen FC & Flanagan JG IMP2 axonal localization, RNA interactome, and function in the development of axon trajectories. Development 143, 2753–2759 (2016). [PubMed: 27385015]
46. Pastrana E, Cheng LC & Doetsch F. Simultaneous prospective purification of adult subventricular zone neural stem cells and their progeny. Proc Natl Acad Sci U S A 106, 6387–6392 (2009). [PubMed: 19332781]
47. Shah PT et al. Single-Cell Transcriptomics and Fate Mapping of Ependymal Cells Reveals an Absence of Neural Stem Cell Function. Cell 173, 1045–1057 e1049 (2018). [PubMed: 29727663]
48. Li B, Carey M. & Workman JL The role of chromatin during transcription. Cell 128, 707–719 (2007). [PubMed: 17320508]
49. Huang C. & Wu JC Epigenetic Modulations of Induced Pluripotent Stem Cells: Novel Therapies and Disease Models. Drug Discov Today Dis Models 9, e153–e160 (2012). [PubMed: 23646061]
50. Sun F. et al. Promoter-Enhancer Communication Occurs Primarily within Insulated Neighborhoods. Mol Cell 73, 250–263 e255 (2019). [PubMed: 30527662]
51. Chronis C. et al. Cooperative Binding of Transcription Factors Orchestrates Reprogramming. Cell 168, 442–459 e420 (2017). [PubMed: 28111071]
52. Park J, Lee K, Kim K. & Yi SJ The role of histone modifications: from neurodevelopment to neurodiseases. Signal Transduct Target Ther 7, 217 (2022). [PubMed: 35794091]
53. Buenrostro JD, Wu B, Chang HY & Greenleaf WJ ATAC-seq: A Method for Assaying Chromatin Accessibility Genome-Wide. Curr Protoc Mol Biol 109, 21 29 21–21 29 29 (2015).
54. Cho YW et al. PTIP associates with MLL3- and MLL4-containing histone H3 lysine 4 methyltransferase complex. J Biol Chem 282, 20395–20406 (2007). [PubMed: 17500065]
55. Dhar SS et al. Trans-tail regulation of MLL4-catalyzed H3K4 methylation by H4R3 symmetric dimethylation is mediated by a tandem PHD of MLL4. Genes Dev 26, 2749–2762 (2012). [PubMed: 23249737]
56. Huisman C. et al. The histone H3-lysine 4-methyltransferase Mll4 regulates the development of growth hormone-releasing hormone-producing neurons in the mouse hypothalamus. Nat Commun 12, 256 (2021). [PubMed: 33431871]
57. Sridharan R. et al. Proteomic and genomic approaches reveal critical functions of H3K9 methylation and heterochromatin protein-1gamma in reprogramming to pluripotency. Nat Cell Biol 15, 872–882 (2013). [PubMed: 23748610]
58. Miranda CJ et al. Aging brain microenvironment decreases hippocampal neurogenesis through Wnt-mediated survivin signaling. Aging Cell 11, 542–552 (2012). [PubMed: 22404871]
59. Sun D. et al. Epigenomic profiling of young and aged HSCs reveals concerted changes during aging that reinforce self-renewal. Cell Stem Cell 14, 673–688 (2014). [PubMed: 24792119]
60. Liu L. et al. Chromatin modifications as determinants of muscle stem cell quiescence and chronological aging. Cell Rep 4, 189–204 (2013). [PubMed: 23810552]

61. Maybury-Lewis SY et al. Changing and stable chromatin accessibility supports transcriptional overhaul during neural stem cell activation and is altered with age. Aging Cell 20, e13499 (2021). [PubMed: 34687484]

62. Sun Y. et al. Neurogenin promotes neurogenesis and inhibits glial differentiation by independent mechanisms. Cell 104, 365–376 (2001). [PubMed: 11239394]

63. Sun H. et al. Quantitative integration of epigenomic variation and transcription factor binding using MAmotif toolkit identifies an important role of IRF2 as transcription activator at gene promoters. Cell Discov 4, 38 (2018). [PubMed: 30002873]

64. Liu Z, Scannell DR, Eisen MB & Tjian R. Control of embryonic stem cell lineage commitment by core promoter factor, TAF3. Cell 146, 720–731 (2011). [PubMed: 21884934]

65. Corenblum MJ et al. Reduced Nrf2 expression mediates the decline in neural stem cell function during a critical middle-age period. Aging Cell 15, 725–736 (2016). [PubMed: 27095375]

66. Anandhan A, Kirwan KR, Corenblum MJ & Madhavan L. Enhanced NRF2 expression mitigates the decline in neural stem cell function during aging. Aging Cell 20, e13385 (2021). [PubMed: 34128307]

67. Obernier K. & Alvarez-Buylla A. Neural stem cells: origin, heterogeneity and regulation in the adult mammalian brain. Development 146 (2019).

68. Kaise T. et al. Functional rejuvenation of aged neural stem cells by Plagl2 and anti-Dyrk1a activity. Genes Dev 36, 23–37 (2022). [PubMed: 34916302]

69. Shan Q, Hu Y, Chen S. & Tian Y. Nucleus accumbens dichotomically controls social dominance in male mice. Neuropsychopharmacology 47, 776–787 (2022). [PubMed: 34750567]

70. Guo W, Patzlaff NE, Jobe EM & Zhao X. Isolation of multipotent neural stem or progenitor cells from both the dentate gyrus and subventricular zone of a single adult mouse. Nat Protoc 7, 2005–2012 (2012). [PubMed: 23080272]

71. Livak KJ & Schmittgen TD Analysis of relative gene expression data using real-time quantitative PCR and the 2(-Delta Delta C(T)) Method. Methods 25, 402–408 (2001). [PubMed: 11846609]

72. Zhang Y. et al. Model-based analysis of ChIP-Seq (MACS). Genome Biol 9, R137 (2008). [PubMed: 18798982]

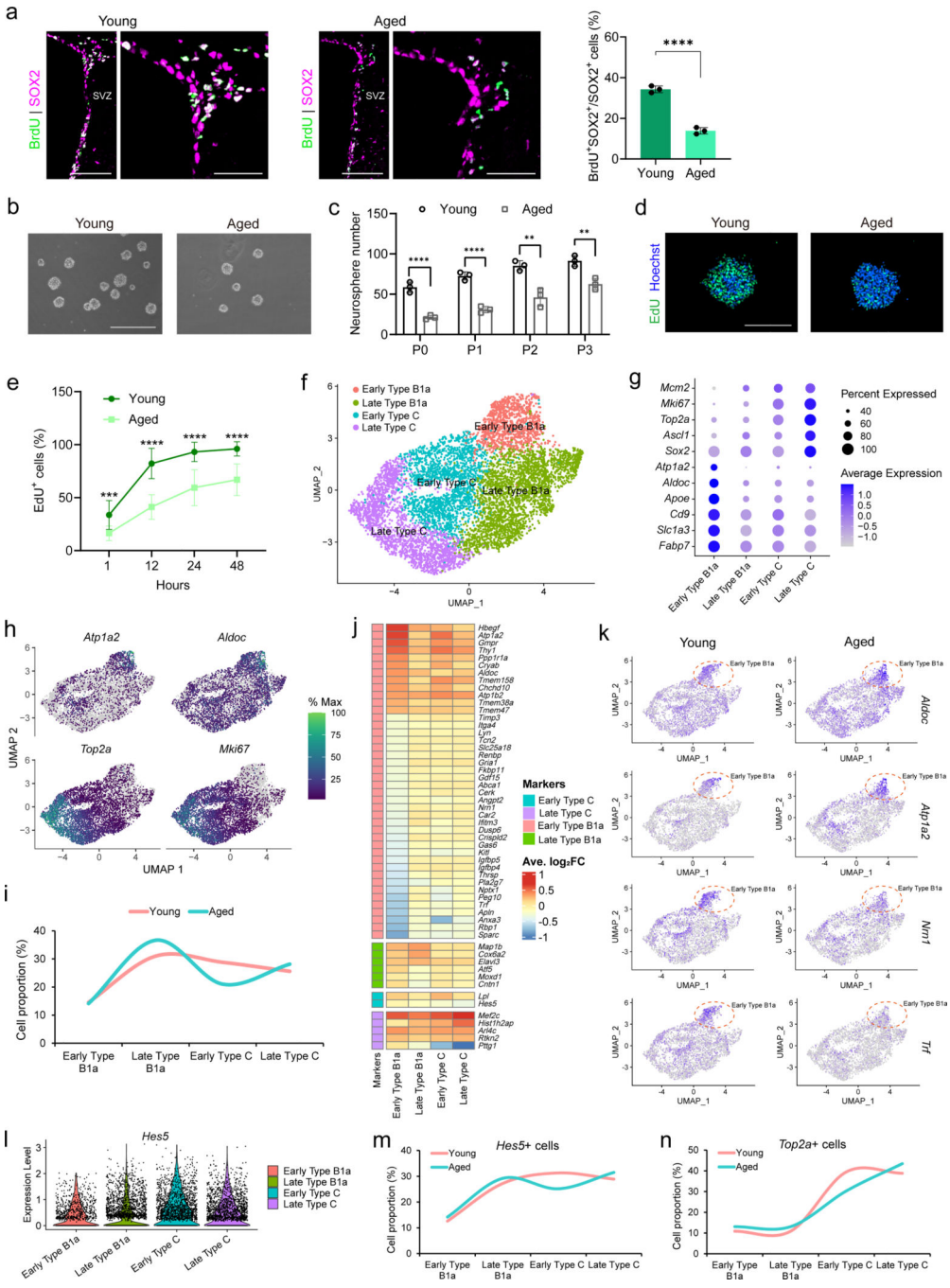

Fig. 1: Generation efficacy of proliferative NSPCs decreases in the aging brain.

a, Confocal microscopy images showing immunofluorescence co-labeling of BrdU and SOX2 in the brain SVZ of young and aged mice. Scale bar, 100 μm. The scale bar in the higher magnification image measures 50 μm. Quantification data was plotted in the bar chart. Three mice per group. Eight sections per mouse. $P = 0.0001$. **b,** Representative images of neurospheres formed by primary NSPCs isolated from the SVZ of young and aged mice, respectively. Scale bar, 1000 μm. The SVZ tissues were pooled from six mice per group. **c,** Quantification of neurospheres formed by different passages of NSPCs. P1–3

neurospheres were generated by seeding equal numbers of young or aged NSPCs from the preceding culture passage, excluding P0 neurospheres derived from the SVZ. n = 3 independent experiments. 18 microscopic fields per age group. P0: $P = 0.0008$, P1: $P = 0.0004$, P2: $P = 0.0053$, P3: $P = 0.0065$. **d,** EdU incorporation assay of young and aged NSPC-derived neurospheres. Hoechst 33342 (Blue) marks nuclei. Scale bar, 200 μm. **e,** Time-course quantification of EdU labeling in young and aged groups (% EdU vs. Hoechst). n = 10. 1hour: $P = 1.04E-03$, 12hour: $P = 4.36E-06$, 24hour: $P = 1.88E-05$, 48hour: $P = 8.70E-05$. **f,** Uniform manifold approximation and projection (UMAP) plot of NSPCs from young and aged mice. Cells are colored by cell types and activation states. **g,** Dot plots showing the expression of NSPC activation and quiescence markers, as well as lineage markers. **h,** Gene expression of quiescence markers (*Atp1a2* and *Aldoc*) and activation markers (*Top2a* and *Mki67*) visualized on UMAP plots. **i,** Percentage of cell population from early type B1a to late type C cells per age group. **j,** Heatmap of marker genes in each NSPC cluster and the average $\log_2$ fold change of expression in aged versus young NSPC populations. **k,** UMAP plots of representative DE markers of early type B1a in young and aged NSPCs. **l,** Violin plots of *Hes5* gene expression in the four clusters of NSPCs. **m,n,** Percentage of *Hes5*-positive and *Top2a*-positive cell populations within the four clusters of NSPCs for each age group. Error bars are mean ± SD for a, c, and e. Statistical analysis in all graphs was performed using an unpaired two-sided Student's *t-test*.

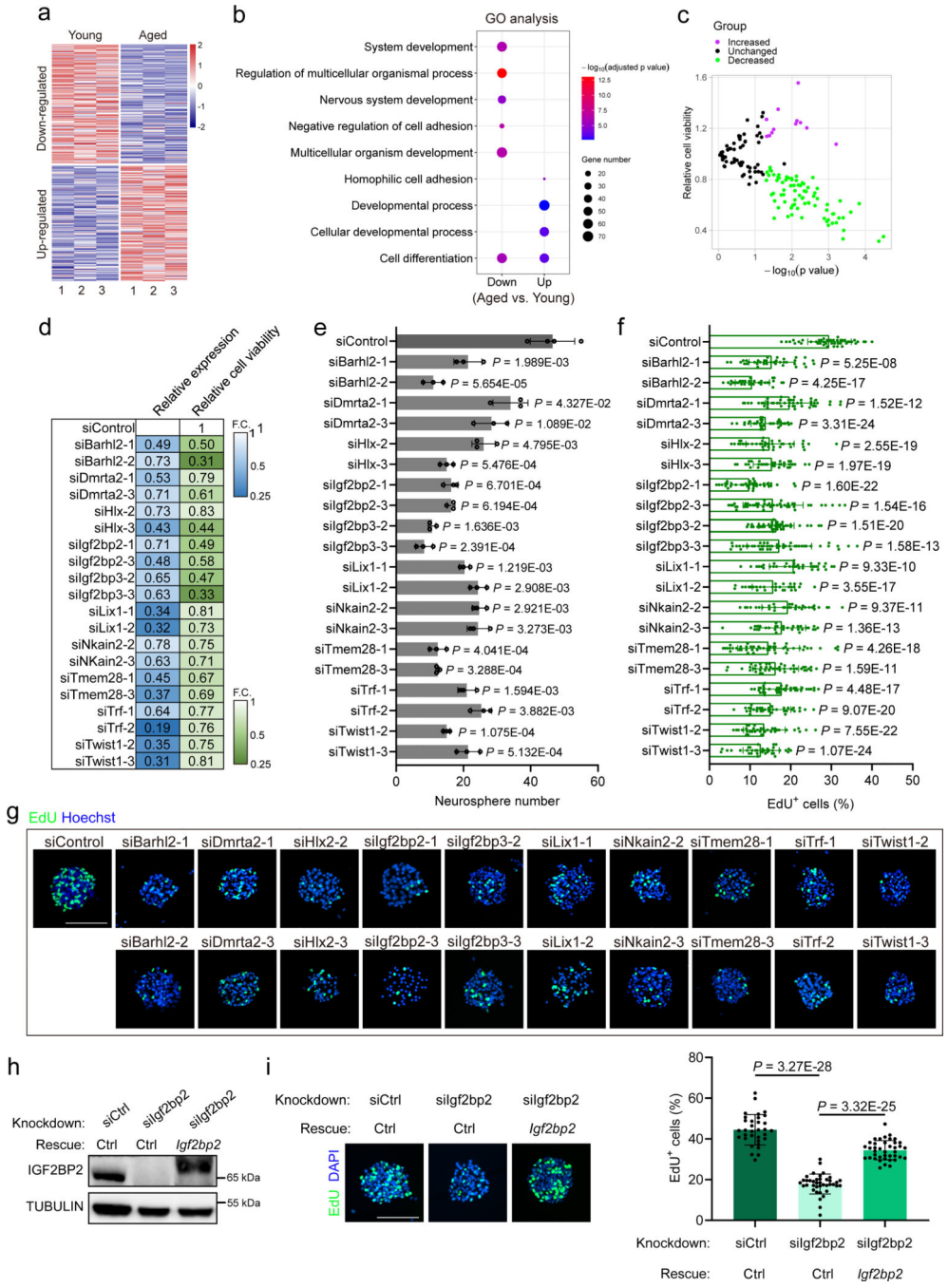

Fig. 2: Downregulation of age-dependent genes drives NSPC aging.

a, Heatmap of down-regulated and up-regulated genes in aged versus young NSPCs. Values of log2(FPKM) from three replicates of RNA-seq data are plotted. **b,** Gene ontology analysis of the down-regulated and up-regulated genes as in (a). Two-sided Hypergeometric test. **c,** Dot plot showing relative cell viability of NSPCs (siRNA group vs. siControl group) 48 hours after siRNA transfection. n = 3 independent experiments. **d,** Heatmap of representative siRNAs that significantly decrease the expression of target genes and the cell viability of NSPCs. The relative expression of genes was analyzed by qPCR from

three independent experiments (siRNA group vs. siControl group, $P < 0.05$, p-values are provided in the source data). **e,** Quantification of neurospheres formed by single NSPCs 48 hours post-transfection of siRNAs as indicated. n = 4 independent experiments for siControl group. n = 3 independent experiments for siRNA group. **f,** EdU incorporation assay with young NSPC-derived neurospheres 48 hours post-transfection of siRNAs. Data are plotted with the percentage of EdU-positive cells versus Hoechst-positive cells in each neurosphere. siControl n = 45, siBarhl2–1 n =37, siBarhl2–2 n = 31, siDmrta2–1 n = 47, siDmrta2–3 n = 35, siHlx-2 n = 38, siHlx-3 n = 33, siIgf2bp2–1 n = 38, siIgf2bp2–3 n = 45, siIgf2bp3–2 n = 41, siIgf2bp3–3 n = 47, siLix1–1 n = 37, siLix1–2 n = 31, siNkain2–2 n = 32, siNkain2–3 n = 31, siTmem28–1 n = 47, siTmem28–3 n = 44, siTrf-1 n = 39, siTrf-2 n = 34, siTwist1–2 n = 34, siTwist1–3 n = 35. **g,** Representative images of EdU labeling of NSPC-derived neurospheres as in (f). Hoechst (blue) marks nuclei. Scale bar, 100 μm. **h,** Western blot of IGF2BP2 protein in the gene knockdown and rescue groups. n = 3 independent experiments. **i,** Representative images of neurospheres treated with knockdown of *Igf2bp2* with and without expression rescue of *Igf2bp2*. Control of rescue was infected with adenovirus without expressing *Igf2bp2*. EdU labeling of neurospheres was performed 48 hours post-transfection. DAPI (blue) marks nuclei. Scale bar, 100 μm. Quantification data are showed in the bar chart with the percentage of EdU-positive versus DAPI-positive cells in each neurosphere. n > 35. Error bars are mean ± SD for e, f, and i. Two-sided Student's *t-tests* for c-f, and i.

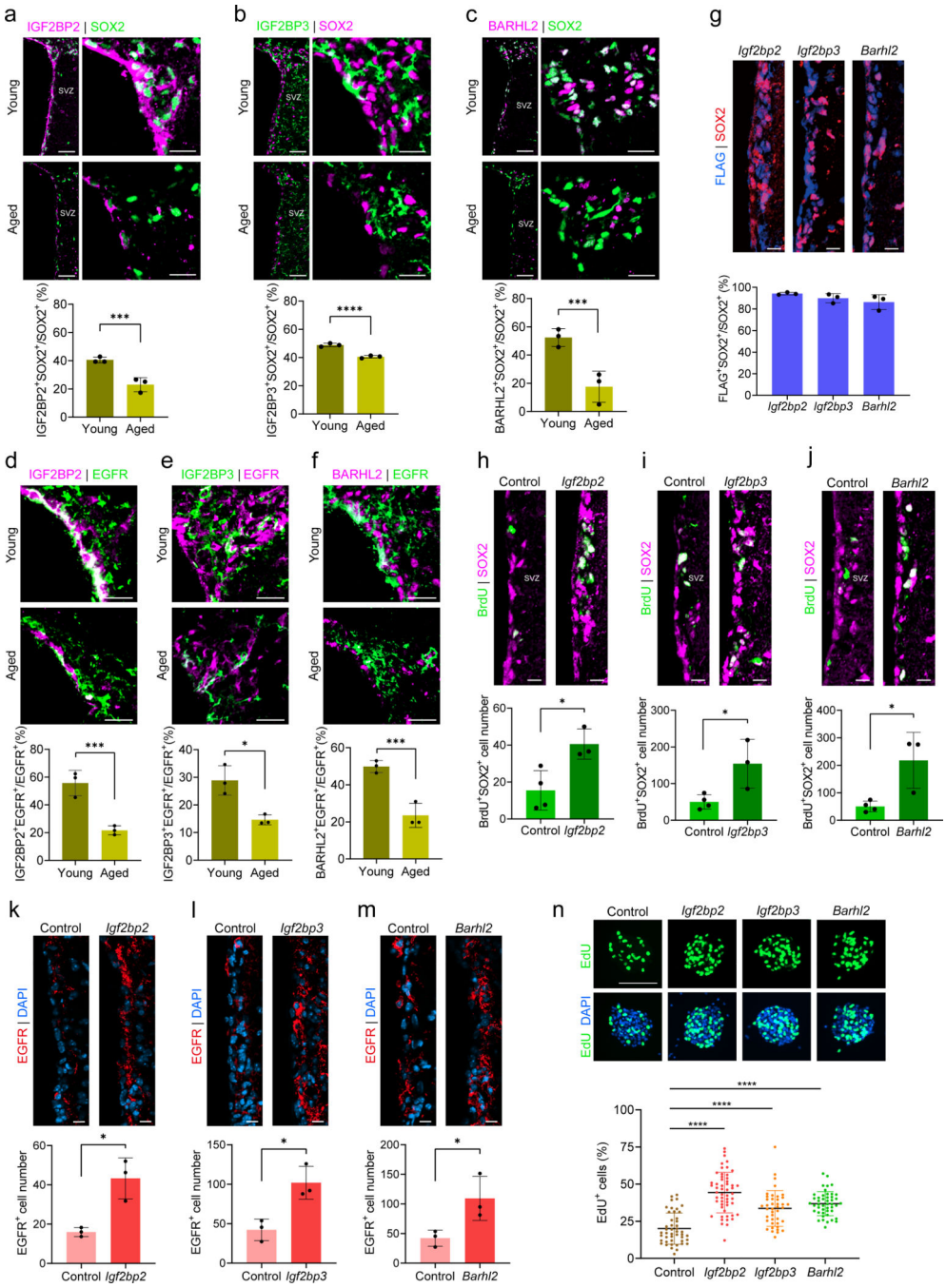

Fig. 3: Age-dependent genes are potential rejuvenation targets for aging NSPCs.

a-c, Confocal fluorescence images from the SVZ of young and aged mice show the immunofluorescence co-labeling of IGF2BP2 (a), IGF2BP3 (b), and BARHL2 (c) with SOX2. Scale bar, 50 μm. The right panel displays a higher magnification image with a scale bar of 20 μm. Double-positive cells were quantified in the lateral, dorsolateral, and dorsal SVZ. The percentage of these double-positive cells versus SOX2+ cells was plotted below the corresponding images. Three mice per group. Four sections per mouse. (a): $P = 0.0049$, (b): $P = 0.0007$, (c): $P = 0.0022$. *** $P < 0.005$. **** $P < 0.001$. **d-f,** Confocal fluorescence

images from the SVZ of young and aged mice show the immunofluorescence co-labeling of IGF2BP2 (d), IGF2BP3 (e), and BARHL2 (f) with EGFR. Scale bar, 20 μm. Double-positive cells were quantified in the lateral, dorsolateral, and dorsal SVZ. The percentages of these double-positive cells versus EGFR+ cells were plotted below images. Three mice per group. Four sections per mouse. (d): $P = 0.0037$, (e): $P = 0.0117$, (f): $P = 0.0033$. * $P < 0.05$. *** $P < 0.005$. **g,** Confocal fluorescence images showing the co-labeling of FLAG and SOX2 in the SVZ of aged mice after the overexpression of FLAG-tagged *Igf2bp2*, *Igf2bp3*, and *Barhl2*. Scale bar, 10 μm. Double-positive cells were quantified in the lateral and dorsolateral SVZ regions. Three mice per group. Six sections per mouse. **h-j,** Confocal fluorescence images show the increased number of activated NSPCs in the SVZ of aged mice after the overexpression of *Igf2bp2* (h), *Igf2bp3* (i), and *Barhl2* (j). Mice were injected intraperitoneally with BrdU two weeks after gene transduction. Control mice were injected with control adenovirus without expressing these three genes. Scale bar, 10 μm. The average number of BrdU+SOX2+ NSPCs per group was plotted blow the images. Double-positive cells were quantified within the lateral and dorsolateral SVZ in each section. A total of six sections per mouse, spaced at 120 μm intervals along the rostrocaudal axis of the SVZ, were used for cell counting. Four mice per control group. Three mice per gene overexpression group. (h): $P = 0.0235$, (i): $P = 0.0285$, (j): $P = 0.0211$. * $P < 0.05$. **k-m,** Overexpression of *Igf2bp2*, *Igf2bp3*, and *Barhl2* increases the number of EGFR-positive cells in the SVZ of aged mice. Cells in the SVZ were co-labeled with EGFR and DAPI. Scale bar, 10 μm. EGFR-positive cells were quantified within the lateral and dorsolateral SVZ in each section. The average number of EGFR+ cells per group was plotted blow the images. Three mice per group. Six sections per mouse. (k): $P = 0.0114$, (l): $P = 0.0142$, (m): $P = 0.0424$. * $P < 0.05$. **n,** EdU labeling of aged NSPC-formed neurospheres 48 hours post-transduction of adenovirus encoding *Igf2bp2*, *Igf2bp3*, and *Barhl2*, respectively. Scale bar, 100 μm. Data are plotted with % EdU+ vs. DAPI+ cells in each neurosphere. Control $n = 46$, *Igf2bp2* $n = 53$, *Igf2bp3* $n = 41$, *Barhl2* $n = 46$. *Igf2bp2:* $P = 3.46E\text{-}16$, *Igf2bp3*: $P = 2.31E\text{-}07$, *Barhl2*: $P = 2.08E\text{-}13$. **** $P < 0.001$. Error bars are mean ± SD in all graphs. Statistical analysis in all graphs was performed using an unpaired two-sided Student's *t-test*.

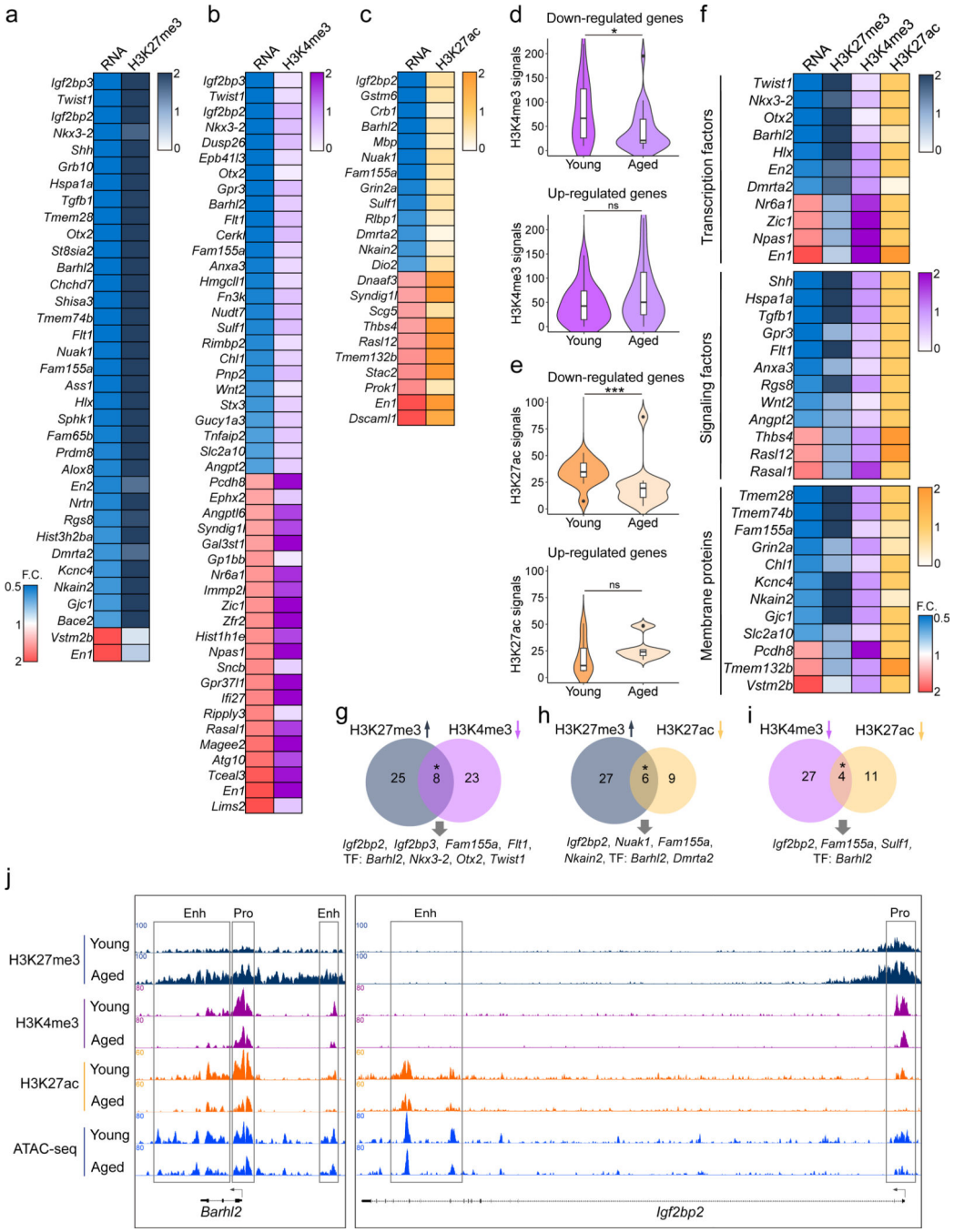

Fig. 4: Changes in histone modifications at gene regulatory elements are related to transcriptional dysregulation of NSPC aging.

a, b, Heatmaps showing fold changes of average ChIP-seq signals of H3K27me3 and H3K4me3 at the promoters of age-dependent genes and the change of their RNA level (Aged vs. Young, FC > 1.5). **c,** Heatmap showing fold change of average H3K27ac signals at the enhancers of age-dependent genes and the change of their RNA level **d,** Average signals of H3K4me3 at the promoters of 26 age-dependent down-regulated genes and 22 up-regulated genes in young and aged NSPCs. Two-sided Wilcoxon rank sum test, * p-value

= 0.0101; ns: p-value = 0.5186. Down-regulated genes n = 26; up-regulated genes n = 22 from 2 independent experiments. The box represents the interquartile range (IQR) with its lower and upper hinges denoting the 25th and 75th percentiles, respectively, and a horizontal line for the median (Centre = 66.51 in young group of down-regulated genes; Centre = 27.47 in aged group of down-regulated genes; Centre = 42.62 in young group of up-regulated genes; Centre = 50.3 in aged group of up-regulated genes), while the whiskers extend up to 1.5 times the IQR from these quartiles. **e,** Average signals of H3K27ac at the enhancers of 13 age-dependent down-regulated genes and 10 up-regulated genes in young and aged NSPCs (Two-sided Wilcoxon rank sum test, *** p-value = 0.0028; ns: p-value = 0.1405). Down-regulated genes n = 13; up-regulated genes n = 10 from 2 independent experiments. The box represents the interquartile range (IQR) with its lower and upper hinges denoting the 25th and 75th percentiles, respectively, and a horizontal line for the median (Centre = 34.62 in young group of down-regulated genes; Centre = 19.38 in aged group of down-regulated genes; Centre = 11.19 in young group of up-regulated genes; Centre = 24.07 in aged group of up-regulated genes), while the whiskers extend up to 1.5 times the IQR from these quartiles. **f,** Functional classification of age-dependent genes with changes of histone modifications at gene promoters (H3K27me3 and H3K4me3) and enhancers (H3K27ac). **g-i,** Venn diagrams show the overlap of age-dependent genes displaying cocurrent changes in histone modifications at the promoters and enhancers in aged vs. young NSPCs. The asterisk denotes significant overlap determined by two-sided hypergeometric test, with p-value of 8.410e-19 for g, 2.114e-13 for h, and 1.064e-08 for i. **j,** Browser tracks show examples of age-dependent changes of histone modifications and ATAC-seq signals at the promoters and enhancers of age-dependent genes.

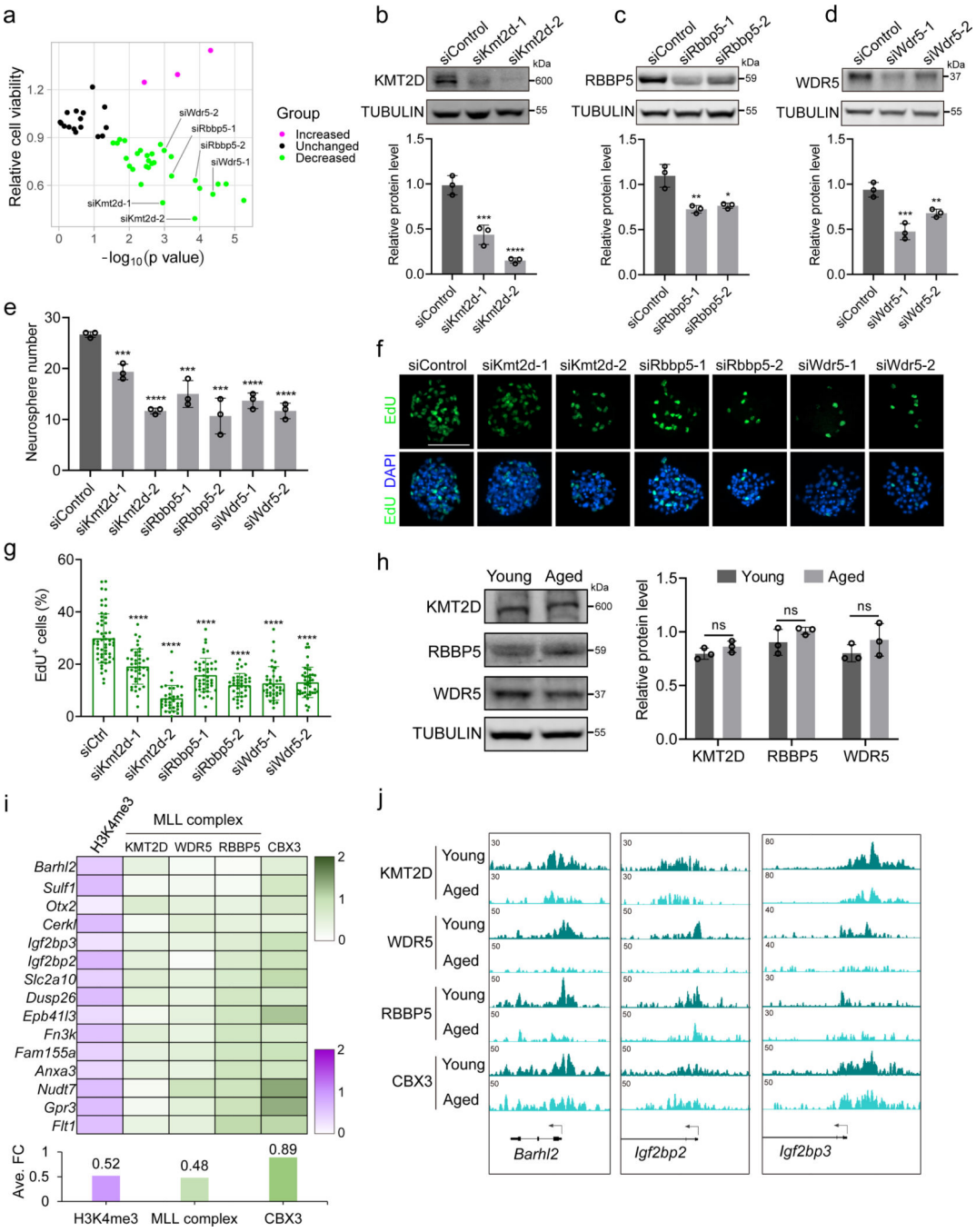

Fig. 5: Identification of MLL complex as a key epigenetic regulator in functional decline of aging NSPCs.

a, Dot plot showing relative cell viability of NSPCs 48 hours after siRNA transfection.

b-d, Western blot analyses of KMT2D, RBBP5, and WDR5 protein levels 48 hours after siRNA transfection in primary young NSPCs. Bar chart shows relative protein level of each MLL complex subunit versus TUBULIN by measuring the blot signals with the software Image J (National Institutes of Health). n = 3. siKmt2d-1: $P = 0.0033$, siKmt2d-2: $P = 0.0002$. siRbbp5–1: $P = 0.0086$. siRbbp5–2: $P = 0.0114$. siWdr5–1: $P = 0.0026$. siWdr5–2:

P = 0.0081. * *P* < 0.05. ** *P* < 0.01. *** *P* < 0.005. **** *P* < 0.001. **e,** Quantification of NSPC-formed neurospheres 48 hours post-transfection of siRNAs as indicated. n = 3 independent experiments. siKmt2d-1: *P* = 0.0016. siKmt2d-2: *P* = 1.52E-05. siRbbp5–1: *P* = 0.0017. siRbbp5–2: *P* = 0.0015. siWdr5–1: *P* = 0.0002. siWdr5–2: *P* = 9.12E-05. *** *P* < 0.005. **** *P* < 0.001. **f,** Representative images of EdU labeling of young NSPC-derived neurospheres 48 hours after siRNA transfection. DAPI (blue) marks nuclei. Scale bar, 100 μm. **g,** Quantification of EdU labeling in young NSPC-derived neurospheres 48 hours post-transfection of siRNAs as indicated. Data are plotted with the percentage of EdU-positive cells versus DAPI-positive cells in each neurosphere. siCtrl n = 55, siKmt2d-1 n = 42, siKmt2d-2 n = 36, siRbbp5–1 n = 45, siRbbp5–2 n = 39, siWdr5–1 n = 40, siWdr5–2 n = 43. siKmt2d-1: *P* = 9.34E-09, siKmt2d-2: *P* = 3.63E-23, siRbbp5–1: *P* = 1.89E-13, siRbbp5–2: *P* = 1.70E-18, siWdr5–1: *P* = 2.07E-16, siWdr5–2: *P* = 3.43E-17. **** *P* < 0.001. **h,** Western blot of endogenous protein levels of KMT2D, RBBP5, and WDR5 from primary young and aged NSPC nuclear extracts. The blot signals were measured by Image J and plotted in the bar chart showing the relative protein level of each MLL complex subunit versus TUBULIN in the young and aged cells. n = 3 independent experiments. **i,** Heatmap showing fold change of ChIP-seq signals of H3K4me3, MLL complex subunits, and CBX3 at each promoter of age-dependent gene in aged versus young NSPCs. Bar chart below shows the average fold changes of H3K4me3, MLL complex, and CBX3 signals at all the above promoters in aged versus young NSPCs. **j,** Browser tracks of *Barhl2*, *Igf2bp2*, and *Igf2bp3* TSS regions with ChIP-seq signals of MLL complex and CBX3 in young and aged NSPCs. Error bars are mean ± SD for b-e, g, and h. Statistical analysis in all graphs was performed using a two-sided Student's *t-test*.

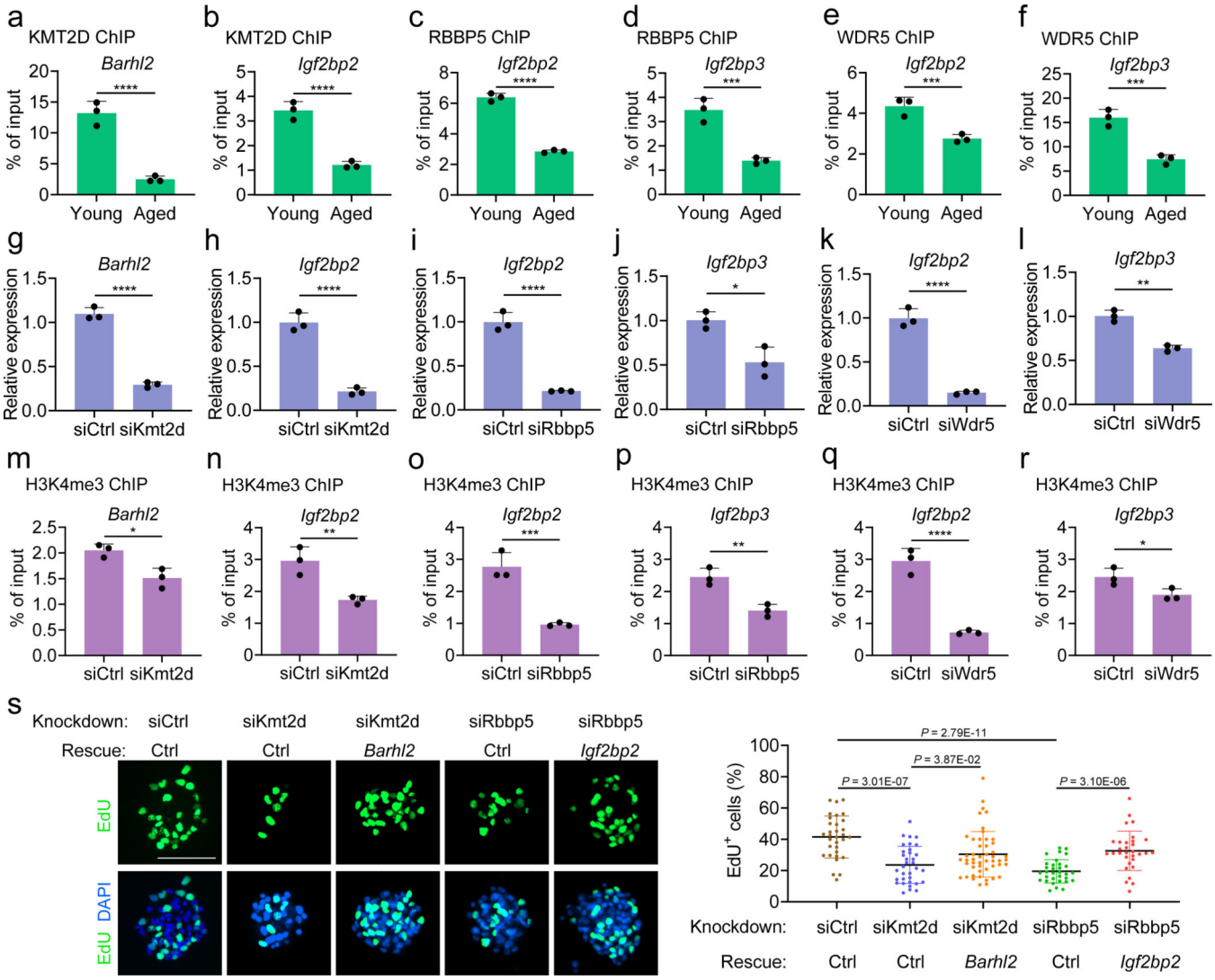

Fig. 6: Loss of function of MLL complex results in transcriptional and epigenetic inactivation of age-dependent genes.

a-f, ChIP-qPCR data showing enrichment of MLL complex at the promoters of *Barhl2*, *Igf2bp2*, and *Igf2bp3* in young and aged NSPCs. $n = 3$ independent assays. (a): $P = 0.0007$, (b): $P = 0.0006$, (c): $P = 2.76E-05$, (d): $P = 0.0019$, (e): $P = 0.0047$, (f): $P = 0.0017$.

g-l, Real-time qPCR analysis of relative expression of genes in MLL-complex-knockdown versus control cells. Young NSPCs were transfected with siRNAs as indicated. Total RNAs of the cells were isolated and reverse-transcribed into cDNAs for qPCR analysis 40 hours post-transfection. $n = 3$ independent assays. (g): $P = 5.71E-05$, (h): $P = 0.0003$, (i): $P = 0.0002$, (j): $P = 0.0136$, (k): $P = 0.0002$, (l): $P = 0.0011$. **m-r,** ChIP-qPCR data showing changes of H3K4me3 signals at the promoters of *Barhl2*, *Igf2bp2*, and *Igf2bp3* upon knockdown of MLL complex in young NSPCs, as compared to the control groups. Cells were used for ChIP assay 40 hours after siRNA transfection. $n = 3$ independent assays. Unpaired two-sided Student's *t-test* for data in (a-r). (m): $P = 0.0146$, (n): $P = 0.0094$, (o): $P = 0.0022$, (p): $P = 0.0062$, (q): $P = 0.0006$, (r): $P = 0.0461$. * $P < 0.05$. ** $P < 0.01$. *** $P < 0.005$. **** $P < 0.001$. **s,** Adenovirus-mediated expression of *Barhl2* and *Igf2bp2*

gene in *Kmt2d*-knockdown and *Rbbp5*-knockdown young NSPCs, respectively. Control of rescue was infected with adenovirus without expressing *Barhl2* and *Igf2bp2*. EdU labeling was performed 48 hours post-transfection. Scale bar, 100 μm. Quantification data are plotted with the percentage of EdU-positive versus DAPI-positive cells in each neurosphere. siCtrl + Ctrl $n = 32$, siKmt2d + Ctrl $n = 34$, siKmt2d + *Barhl2* $n = 50$, siRbbp5 + Ctrl $n = 32$, siRbbp5 + *Igf2bp2* $n = 31$. Error bars are mean ± SD in all the graphs. Statistical analysis in all graphs was performed using a two-sided Student's *t-test*.